# 15

# Photonic Crystal for Polarization Rotation

Bayat and Baroughi
*South Dakota State University*
*USA*

## 1. Introduction

Due to the unique guiding properties of photonic crystal (PC) structure, such as sharp low loss bends, it is considered one of the main contenders of a compact optical integrated circuit (OIC). PC is foreseen as the next generation of hybrid photonic-electronic integrated circuit. However, one of the main issues in implementation of a PC based OIC is its strong polarization dependence guiding behavior.

The components of optical integrated circuit exhibit strong polarization dependence behavior which translates into their random response to random polarizations. One approach to render the polarization sensitivity of an optical integrated circuit is to eliminate the randomness of the input polarization by splitting it into two orthogonal polarizations (TE, TM) and rotating one of the polarizations; thus, single polarization is realized on the chip (Barwicz et al., 2007). The focus of this chapter is to implement PC based polarization rotator which is capable of rotating the polarization of light to an arbitrary angle. The large birefringence in PC structure leads to a small optical path difference between the two polarizations which can result in realization of ultra-compact polarization rotators. Ease of fabrication and its compatibility with integrated PC technology is considered another main advantage of the PC based polarization rotator. This chapter is organized as follows. In Sec.2, an overview on the passive polarization rotators is given. In Sec. 3, a novel polarization rotator structure is introduced and designed. Fabrication and characterization of the PC based polarization rotator are discussed in Sec. 4 and Sec. 5, respectively.

## 2. An overview on passive polarization rotators

Passive polarization rotator structures are mostly composed of geometrically asymmetric structures where the symmetry of the structure is disturbed so that two orthogonal polarizations could be coupled to each other. Imposing asymmetry into a symmetric waveguide structure leads to a perturbation in the primary waveguide axes, depicted in Fig.1, where $E_f$ and $E_s$ are projected fields on fast and slow axes called fast and slow normal modes, respectively. They travel with different speeds resulting in phase delay between the two components. For the phase delay of $180^o$, the power conversion between the two components has reached to its maximum and the propagating distance is called the half-beat length $L_\pi$, defined as (Mrozowski, 1997):

$$L_\pi = \frac{\pi}{\beta_s - \beta_f} = \frac{\pi}{(n_s - n_f)k_0} = \frac{\lambda}{2(n_s - n_f)} \tag{1}$$

Where $\beta_s$ and $\beta_f$ are the propagation constants of slow and fast modes, and $n_s$ and $n_f$ are corresponding effective refractive indices, respectively. The process of polarization rotator in geometrically asymmetric structure can be explained with more details as follows. According to Fig. 1(b), the transverse component of the normal modes of for example the asymmetric loaded rib waveguide (Shani et al., 1991) can be expressed as following, where $\varphi$ is the optical perturbation angle and $E_s$ and $E_f$ are slow and fast modes, respectively:

$$E_s = \cos\varphi\hat{x} - \sin\varphi\hat{y} \tag{2.a}$$

$$E_f = \sin\varphi\hat{x} + \cos\varphi\hat{y} \tag{2.b}$$

Assuming that the input wave is x-polarized, it can be expressed as the combination of $E_s$ and $E_f$ as following:

$$E_i = \cos\varphi\, e^{-j\beta_s z}E_s + \sin\varphi\, e^{-j\beta_f z}E_f \tag{3}$$

At half-beat length long, the slow and fast modes become out of phase resulting in destructive interference between the two modes. Thus, at $z=L_\pi$, the total field become:

$$E_{o1} = \cos\varphi E_s - \sin\varphi E_f \tag{4}$$

Substituting equ. (2) into equ. (4) results in:

$$E_{o1} = \cos 2\varphi\hat{x} - \sin 2\varphi\hat{y} \tag{5}$$

Thus, at $z=L_\pi$ the input wave has been rotated by 2φ with respect to x-axis; depicted in Fig. 1 (c). To avoid the reversal of power conversion and synchronize the power conversion, where $\varphi<45^o$, the top loaded layer of the asymmetric loaded layer rib waveguide must be inverted w.r.t the center of rib waveguide at $z=L_\pi$ where z is the propagation direction, Fig. 1(a). At the end of the next brick, the polarization of the input signal has been rotated by 4φ; depicted in Fig 1(d). The top loaded layers will be arranged periodically and repeated until the total phase shift becomes $90^o$ (Snyder & Love, 1983).

In single section polarization rotator structures, φ is adjusted to $45^o$; so that, $90^o$ polarization rotation could be achieved by only one section.

Several structures of longitudinally variable passive polarization rotators have been reported in literature including: periodic asymmetric loaded rib waveguide (Shani et al., 1991), periodic tilted waveguiding section (Heidrich et al., 1992), periodically loaded strip waveguide (Mertens et al., 1998), cascaded bend waveguides (Van Dam et al., 1996; Liu et al., 1997, 1998a, 1998b) and a mode-evolution-based polarization rotator structure (Watts et al., 2005).

Periodic asymmetric loaded rib waveguide was experimentally demonstrated by Shani. The asymmetric loading of the waveguide would perturb the axes of the primary waveguide. By periodically alternating the loaded layer in longitudinal direction the polarization conversion or rotation will be accumulated coherently. The total length of the device was more than 3 mm. Haung and Mao employed coupled mode theory based on scalar modes to analyze the structure theoretically (Haung & Mao, 1992). Later on, Obayya and at el.

Employed full vectorial analysis based on versatile finite element beam propagation method (VFEBPM) to improve the design and reduce the polarization conversion length to 400 μm at operating wavelength of 1.55 μm (Obayya et al., 2000). Due to the huge size of the device, the design could not be verified with the aid of rigorous numerical methods, three dimensional finite difference time domain method (3D-FDTD).

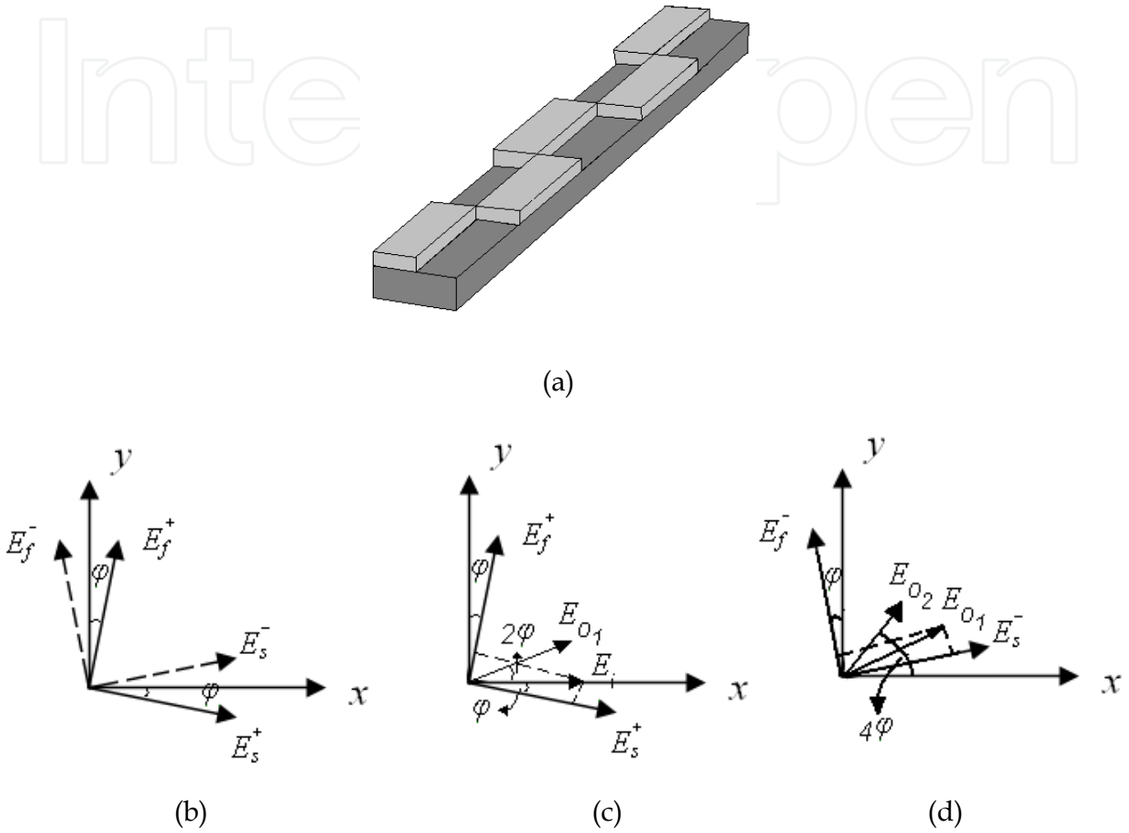


Fig. 1. The sketch of asymmetric loaded rib waveguide and its normal modes (a) asymmetric loaded rib waveguide (b) normal modes of perturbed optical axis ($E_s^+$, $E_f^+$), ($E_s^-$, $E_f^-$) (c) the input electrical field,$E_i$ , and the rotated output field, $E_{o1}$, after propagation distance of $L_п$ (d) the output field after another $L_п$, $E_{o2}$ ($E_s$ and $E_f$ are the slow and fast modes, respectively).

Based on the same idea, tilted waveguiding polarization converter was introduced first by Heidrich (Heidrich et al., 1992). The first device was implemented by laterally tilted InP/GaInAsP rib waveguide on stepped substrate. The total length of the device was more than 7 mm . Later on by improving the design using coupled mode theory and BPM, the more compact device with the total length of 0.9 mm was implemented by Van der Tol. Besides being bulky, the device undertakes huge coupling loss at the junctions between the adjacent periodic sections. To eliminate the loss, single section devices were proposed (Tzolov & Fontaine, 1996; Huang et al., 2000; Rahman et al., 2001). By using angled single section waveguides in InP/InGaAs material system, another type of short polarization rotator was designed and fabricated (El-Refaei & Yevick, 2003).

Silicon based polarization rotators are more attractive in the sense that fabrication process is more compatible with the complementary metal-oxide semiconductor (CMOS) technology. Chen and et al. introduced silicon slanted rib waveguide for polarization rotation (Chen et al., 2003). Deng and et al. implemented slanted wall in Si by wet etching of Silicon <100>; thus, the side wall angle ($52^o$) was not a flexible parameter. The total length of the fabricated device was more than 3 mm which was considered bulky (Deng, 2005). Moreover, the fabrication process of slanted-wall ridge waveguide is not compatible with planar optics circuit.

Recently, Wang and Dai proposed Si nanowire based polarization rotator with asymmetrical cross section, depicted in Fig. 2. The side wall is vertical; thus, it could be realized utilizing dry etching, reactive ion etching (RIE) (Wang & Dai, 2008). They were able to design asymmetric si nanowire device as small as 10 μm. Single mode guiding is required to avoid multimode interface that leads to lower polarization conversion efficiency. However, single mode silicon nanowires are so small that makes the fabrication very difficult and challenging. The fabrication tolerance is very small; thus, the proposed structure is not a robust device in the sense that small fabrication error could diminish the performance of the device. Moreover, to achieve a compact polarization rotator, the height of the loading (h) is 240 nm that is almost half of the thickness of the nanowire (H=500 nm) leading to a huge coupling loss.

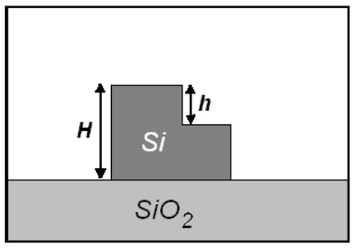


Fig. 2. The sketch of the cross section of asymmetric Si nanowire for polarization rotation application (Wang & Dai, 2008).

Having studied the existing polarization rotators, the major issues are either size or complexity of the structure. To tackle these issues, a PC based polarization rotator is introduced in the following section.

## 3. PC based polarization rotator

### 3.1 Introduction

The two main criteria are compactness and compatibility with planar PC circuit. PC structure was emerged as the best candidate to meet both requirements. PC slab waveguide is highly birefringent and compact; moreover, the fabrication process of the asymmetric loaded PC slab waveguide and integrated planar optical circuits are compatible.

Fig. 3(a) shows the schematic of the proposed polarization rotator. It consists of a single defect line PC slab waveguide. The geometrical asymmetry that is required to couple two orthogonal polarizations to each other was introduced to the upper layer of the defect line. The upper layer is made of the same material as the slab layer etched asymmetrically with

respect to z-axis (propagation direction). Power conversion reversal happens at half beat lengths along the line. In order to avoid power conversion reversal and synchronize the coupling, the upper layer that is half beat length long is alternated on either side of the z-axis with the given period. The proposed structure is described as periodic asymmetric loaded PC slab waveguide. Because of the large birefringence of PC structures, the PC based polarization rotator is expected to be very compact as opposed to periodic asymmetric loaded rib waveguide. Compact structure requires smaller number of loading layers; hence the radiation loss at the junctions between different sections will be reduced.

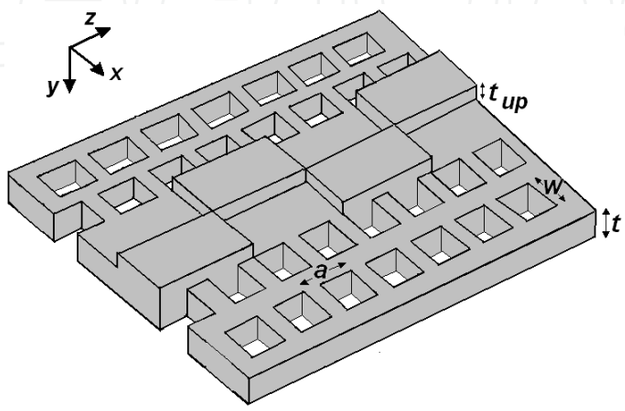


(a)

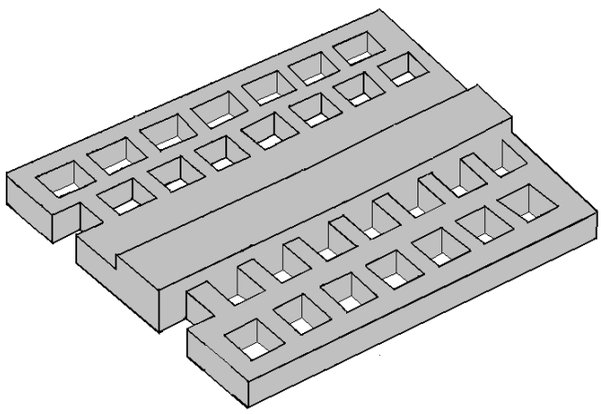

(b)

Fig. 3. The sketch of (a) periodic asymmetric loaded triangular PC slab waveguide (b) asymmetric loaded PC slab waveguide.

Due to the compactness of the structure, a rigorous numerical method, 3D-FDTD can be employed for analysis and simulation. However, for preliminary and quick design an analytical method that provides the approximate values of the structural parameters is preferred. Coupled-mode theory is a robust and well-known method for the analysis of perturbed waveguide structures. Thus, the coupled-mode theory based on semi-vectorial modes was developed for PC structures (Bayat et al., 2009). However, the frequency band of

the modes of the asymmetric loaded PC slab waveguide must be determined prior to the coupled mode analysis. Plane wave expansion method (PWEM) was employed for modal analysis of the asymmetric loaded PC slab waveguide. For coupled mode analysis, the semi-vectorial modes of the asymmetric loaded PC slab waveguide, Fig. 3 (b), were calculated using semi-vectorial beam propagation method (BPM) of RSOFT, version 8.1. Coupled mode theory was employed to calculate the cross coupling between x-polarized and y-polarized waves. To simplify the problem for analytical calculations, instead of circular-hole PC pattern, square-hole PC pattern was employed. The coupled mode theory is an approximate method that provides an estimation of the structural parameters. The combination of the coupled mode theory and PWEM provides the frequency band over which low loss high efficiency polarization rotation is expected to be achieved.

Although, coupled mode theory presents a quick and efficient design methodology; it poses a tedious and error-prone process of discretization along the propagation direction for more complicated geometries such as circular hole PC slab. Thus, another design methodology based on vector-propagation characteristics of normal modes of asymmetric loaded PC slab waveguide was implemented. It can be employed for any arbitrary shape PC slab structure. Normal mode analysis of asymmetric loaded PC slab waveguide provides with fast and slow normal modes of the structure; so that, the half-beat length can be easily calculated (Mrozowki, 1997). The vector-propagation characteristics of normal modes of the asymmetric loaded PC slab waveguide were calculated using 3D-FDTD analysis combined with spatial fourier transform (SFT) of the electric field along the propagation direction. Both coupled-mode analysis and normal mode analysis led to the same results for square shape PC slab waveguide based polarization rotator. To verify the design parameters obtained using coupled mode theory and normal mode analysis, polarization rotator structure was simulated using 3D-FDTD.

Fig. 4 presents the flow chart of the design. It shows the design consists of three main steps. In the first step, the operational frequency band is determined using PWEM analysis. In this step, the thickness of the asymmetric loaded PC slab waveguide is optimized to provide maximum frequency band over which highly efficient polarization conversion is expected to take place. In the second step, coupled mode theory is employed for preliminary design of the polarization rotator. The outputs of this step are the length of top loaded layers (half-beat length) and total number of top loaded layers. Finally, to verify the design parameters obtained using coupled mode theory the 3D-FDTD simulation is performed. Coupled mode theory was developed for square hole geometries. For circular hole PC structure, another design methodology based on 3D-FDTD was developed, shown by 2′ in the figure. As it was explained before, 3D-FDTD analysis of asymmetric loaded PC slab waveguide combined with SFT was employed to obtain the vector-propagation characteristics of the normal modes (slow and fast modes) of the structure. The accuracy of this method can be examined by 3D-FDTD simulation of the polarization rotator structure. In Sec. 3.2, the design methodology has been elaborated. The design and simulation results are presented in Sec. 3.3.

### 3.2 Theory

The schematic of the asymmetric square-hole PC slab polarization rotator is shown in Fig. 3(a). In this structure, the unit cell, the width of the square holes, the thicknesses of silicon

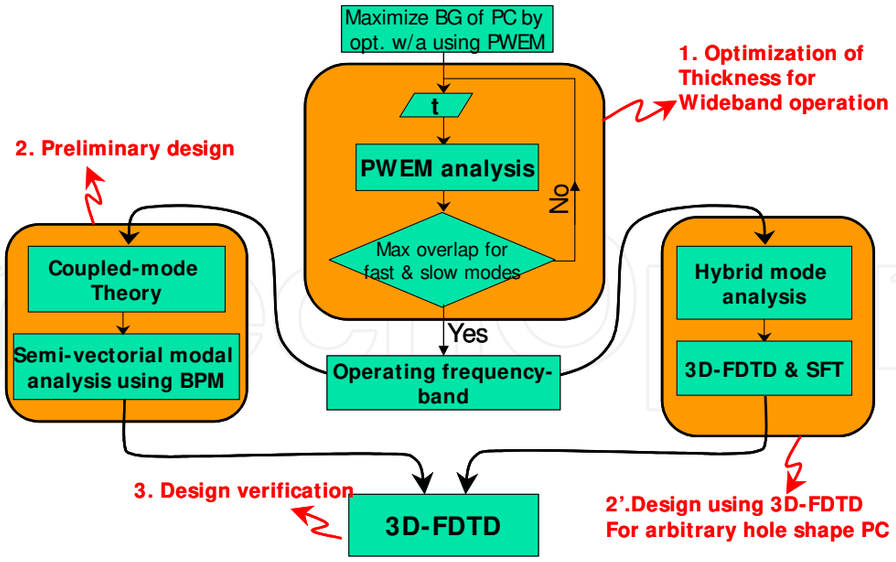


Fig. 4. The flow chart of the design methodology of PC slab waveguide based polarization rotator.

PC slab waveguide and top loaded layer are represented by a, w, t and $t_{up}$, respectively. The top cladding layer is asymmetric with respect to the z-axis (propagation direction) and alternates periodically throughout the propagation direction to synchronize the coupling between the two polarizations. The vector wave equation for the transverse electric field (x-y and z are the transverse and propagation directions, respectively) is given by (Haung et al., 1992):

$$\frac{\partial^2 E_x}{\partial z^2} + \nabla_t^2 E_x + n^2 k^2 E_x = -\frac{\partial}{\partial x}\left(E_x \frac{1}{n^2}\frac{\partial n^2}{\partial x}\right) - \frac{\partial}{\partial x}\left(E_y \frac{1}{n^2}\frac{\partial n^2}{\partial y}\right) \tag{6.a}$$

$$\frac{\partial^2 E_y}{\partial z^2} + \nabla_t^2 E_y + n^2 k^2 E_y = -\frac{\partial}{\partial y}\left(E_x \frac{1}{n^2}\frac{\partial n^2}{\partial x}\right) - \frac{\partial}{\partial y}\left(E_y \frac{1}{n^2}\frac{\partial n^2}{\partial y}\right) \tag{6.b}$$

where, n is the refractive index distribution of the waveguide and $\nabla_t^2$ is the transverse differential operator defined as:

$$\nabla_t^2 = \frac{\partial^2}{\partial x^2} + \frac{\partial^2}{\partial y^2}$$

The vector properties are manifested on the right hand side of equ. (6.a), equ. (6.b); which indicates that the two orthogonal polarizations may be coupled to each other as a result of geometrical asymmetry.

Two approaches including normal mode analysis of the asymmetric loaded PC slab waveguide and coupled mode theory based on semi-vectorial modes were employed to design the polarization rotator structure. Both methods are explained in the following subsections.

### 3.2.1 Normal mode analysis using 3D-FDTD

The first approach to design the polarization rotator structure is to calculate vector-propagation characteristics of normal modes (fast and slow modes) of the asymmetric loaded PC slab waveguide (Fig. 3(b)). The half-beat length and the total number of the loaded layers can be calculated using equ. (1). To obtain modal characteristics of the fast and slow modes of the asymmetric loaded PC slab waveguide, 3D-FDTD method is employed. The propagation constants of x-polarized and y-polarized waves are extracted from 3D-FDTD simulation results using SFT of the electric field along the propagation direction. However, first the frequency band over which slow and fast modes are guided must be determined so that 3D-FDTD simulation could be performed over the aforementioned frequency band. PWEM is employed to obtain the band diagram of the asymmetric loaded PC slab waveguide. To calculate the birefringence of the structure, the effective frequency-dependent index of refraction of the normal modes is to be calculated. To obtain the aforementioned data, the accurate dispersion analysis is carried out, which is based on SFT of the electromagnetic field distribution in the PC slab waveguide along the propagation direction at any point on defect line cross section, the plane normal to the propagation direction ($y$, z). To employ SFT, it is assumed that the electromagnetic field in the PC slab waveguide can be expressed as a modal expansion at the normal plane, as following:

$$E_{\omega}(x,y,z) = \sum_{n,m} E_{n,m,\omega} e^{j\beta_{n,m,\omega} z} \tag{7}$$

where $E_{n,m,\omega}$ and $\beta_{n,m,\omega}$ represent the electric field component and the propagation constant of the $(n,m)^{th}$ mode at frequency ω. The peaks of the SFT spectrum describe the propagating modes of the structure. These peaks are independent of the location, ($x_0$ , $y_0$) and the electromagnetic field components. The effective refractive indices of the modes can be determined by locating these peaks.

Having determined the effective refractive indices of the fast and slow modes, $L_{\pi}$ can be calculated as well as the total number of top loaded layers. The design methodology presented in this subsection requires finding the vector-propagation characteristics of normal modes of asymmetric loaded PC slab waveguide. It is a very general methodology and can be extended to any air hole geometry of PC slab structure as opposed to coupled-mode theory that is more efficient for simple air hole geometry PC structures such as square hole PC slab based polarization rotator. In the following subsection, coupled-mode theory based on semi-vectorial modes of the structure is presented.

### 3.2.2 Coupled-mode theory

Huang and Mao employed similar coupled mode theory based on the scalar modes to analyze polarization conversion in a periodic loaded rib waveguide. In a PC slab waveguide, the propagation characteristics strongly depend on the polarization of the propagating wave leading to a large birefringence (Genereux et al., 2001). However, scalar modal analysis completely ignores the polarization dependence of the wave propagation; thus, it is too simplified to represent the wave propagation inside a PC slab waveguide. Here, coupled mode theory based on semi-vectorial modes of a PC structure was developed to analyze the asymmetric loaded PC slab waveguide. Using semi-vectorial modal analysis,

the polarization dependence of wave propagation has been partially taken into account; thus, the coupling between the two x-polarized and y-polarized waves can be modeled more accurately using coupled mode analysis.

In a triangular lattice PC structure, cross-section varies along the propagation direction within one unit cell. Employing square holes instead of circular holes simplifies the problem of modeling of such structures. According to Fig. 5, the unit cell can be divided into two regions with designated coupling coefficients. Thus, the problem boils down to calculating the coupling coefficients for regions 1 and 2. Semi-vectorial BPM (BPM package of RSOFT) was employed to calculate the semi-vectorial modes of the asymmetric PC slab waveguide shown in Fig. 3(b). The output of BPM analysis were the profile and the propagation constants of the x-polarized and y-polarized modes of the asymmetric loaded PC slab waveguide that were used to calculate the coupling coefficients of the x-polarized and y-polarized waves. Assuming that the profile of the total transverse field in the asymmetric loaded PC slab waveguide is represented as following:

$$E = E_x\hat{x} + E_y\hat{y} \quad = a_x(z)e_x(x,y)e^{-j\beta_x z} + a_y(z)e_y(x,y)e^{-j\beta_y z}\,, \tag{8}$$

Where $e_x(x,y)e^{-j\beta_x z}$ and $e_y(x,y)e^{-j\beta_y z}$ are x- and y-components of electric field of the semi-vectorial solution of wave equation for x-polarized and y-polarized waves, respectively. $\beta_x$ and $\beta_y$ are propagation constants along x and y directions, respectively. Substituting equ. (8) into equ. (6) and multiplying both side of equ. (6.a), and equ. (6.b) by $e^{j\beta_x z}$ and $e^{j\beta_y z}$, respectively, and assuming that the amplitude of the field are slowly varying along z-direction (propagation direction); the following equation is obtained:

$$\begin{aligned} -j2\beta_x e_x \frac{da_x(z)}{dz} + a_x(z)\nabla_t^2 e_x + n^2k^2 a_x(z)e_x - \beta_x^2 a_x(z)e_x = \\ -a_x(z)\frac{\partial}{\partial x}(e_x\frac{1}{n^2}\frac{\partial n^2}{\partial x}) - a_y(z)e^{-j\Delta z}\frac{\partial}{\partial x}(e_y\frac{1}{n^2}\frac{\partial n^2}{\partial y}) \end{aligned} \tag{9.a}$$

$$\begin{aligned} -j2\beta_y e_y \frac{da_y(z)}{dz} + a_y(z)\nabla_t^2 e_y + n^2k^2 a_y(z)e_y - \beta_y^2 a_y(z)e_y = \\ -a_y(z)\frac{\partial}{\partial y}(e_y\frac{1}{n^2}\frac{\partial n^2}{\partial y}) - a_x(z)e^{j\Delta z}\frac{\partial}{\partial y}(e_x\frac{1}{n^2}\frac{\partial n^2}{\partial x}) \end{aligned} \tag{9.b}$$

Where: $\Delta = \beta_y - \beta_x$ ,

By invoking the following assumption:

$$\begin{aligned} \nabla_t^2 e_x + (n^2k^2 - \beta_{ave}^2)e_x = 0 \\ \nabla_t^2 e_y + (n^2k^2 - \beta_{ave}^2)e_y = 0 \end{aligned}\,, \tag{10}$$

Where, $\beta_{ave} = \dfrac{\beta_x + \beta_y}{2}$ ,

A simplified form of equ. (9) is obtained:

$$-j2\beta_x e_x \frac{da_x(z)}{dz} + (\beta_{ave}^2 - \beta_x^2)a_x(z)e_x = \\ -a_x(z)\frac{\partial}{\partial x}(e_x \frac{1}{n^2}\frac{\partial n^2}{\partial x}) - a_y(z)e^{-j\Delta z}\frac{\partial}{\partial x}(e_y \frac{1}{n^2}\frac{\partial n^2}{\partial y}) \tag{11.a}$$

$$-j2\beta_y e_y \frac{da_y(z)}{dz} + (\beta_{ave}^2 - \beta_y^2)a_y(z)e_y = \\ -a_y(z)\frac{\partial}{\partial y}(e_y \frac{1}{n^2}\frac{\partial n^2}{\partial y}) - a_x(z)e^{j\Delta z}\frac{\partial}{\partial y}(e_x \frac{1}{n^2}\frac{\partial n^2}{\partial x}) \tag{11.b}$$

Multiplying both sides of equ. (11.a), and equ. (11.b) by $e_x^*$ and $e_y^*$ (*- conjugate), respectively and integrating over the cross-section, the following coupled mode equations are obtained:

$$\frac{da_x(z)}{dz} = -j\kappa_{xx}a_x(z) - j\kappa_{xy}a_y(z) \\ \frac{da_y(z)}{dz} = -j\kappa_{yy}a_y(z) - j\kappa_{yx}a_x(z) \tag{12}$$

Where:

$$\kappa_{xx} = \frac{(\beta_{ave}^2 - \beta_x^2)\iint e_x^*.e_x dxdy + \iint e_x^*.\frac{\partial}{\partial x}(e_x \frac{1}{n^2}\frac{\partial n^2}{\partial x})dxdy}{2\beta_x \iint e_x^*.e_x dxdy} \tag{13.a}$$

$$\kappa_{xy} = \frac{e^{-j\Delta z}\iint e_x^*.\frac{\partial}{\partial x}(e_y \frac{1}{n^2}\frac{\partial n^2}{\partial y})dxdy}{2\beta_x \iint e_x^*.e_x dxdy} \tag{13.b}$$

$$\kappa_{yy} = \frac{(\beta_{ave}^2 - \beta_y^2)\iint e_y^*.e_y dxdy + \iint e_y^*.\frac{\partial}{\partial y}(e_y \frac{1}{n^2}\frac{\partial n^2}{\partial y})dxdy}{2\beta_y \iint e_y^*.e_y dxdy} \tag{13.c}$$

$$\kappa_{yx} = \frac{e^{j\Delta z}\iint e_y^*.\frac{\partial}{\partial y}(e_x \frac{1}{n^2}\frac{\partial n^2}{\partial x})dxdy}{2\beta_y \iint e_y^*.e_y dxdy} \tag{13.d}$$

$\kappa_{xx}$ and $\kappa_{yy}$ are the self-coupling coefficients; whereas, $\kappa_{xy}$ and $\kappa_{yx}$ refer to cross-coupling coefficients. In equ. (13.a), and equ. (13.c), the second terms were negligible in comparison with the first terms. The coupling coefficients must be solved for both regions 1 and 2 (see Fig. 5), using equ. (13). The distribution of the electric fields in both regions are the same;

where as, the refractive index profile is different as depicted in Fig. 5 leading to different values of coupling coefficients for regions 1 and 2. If the cross-coupling coefficients in both regions 1 and 2 were assumed to be equal ($\kappa_{xy}= \kappa_{yx}= \kappa$), the coupled-mode equations could be solved analytically as presented in equ. (14) below. Nonetheless, numerical methods could be easily implemented for general cases where the cross-coupling coefficients were not equal. Given the exact analytical solution as *A(z)=MA(0)*; where *A* is a column vector for coefficients $a_x$ and $a_y$; the transfer matrix (*M*) is expressed as following:

$$M_{i\pm}=\begin{pmatrix}\cos(\Omega_i z_i)-j\cos(\varphi_i/2)\sin(\Omega_i z_i) & \mp j\sin(\varphi_i/2)\sin(\Omega_i z_i)\\ \mp j\sin(\varphi_i/2)\sin(\Omega_i z_i) & \cos(\Omega_i z_i)+j\cos(\varphi_i/2)\sin(\Omega_i z_i)\end{pmatrix} \quad i=1,2 \tag{14}$$

$$\Omega_i=\sqrt{\delta_i^2+\kappa_i^2}$$

$$\delta_i=\frac{\kappa_{xxi}-\kappa_{yyi}}{2} \tag{15}$$

$$\tan(\varphi_i/2)=\frac{\kappa_i}{\delta_i}$$

The ± signs correspond to the alternative sections of the periodic loading. $z_1$ and $z_2$ are the length of regions 1 and 2 shown in Fig. 5. Assuming that w is the width of a square hole, $z_1$ and $z_2$ are determined as following:

$$z_1=a-w \tag{16.a}$$

$$z_2=w \tag{16.b}$$

Having set $M_1$ and $M_2$ as the transfer matrix of regions 1 and 2, the transfer matrix for one unit cell is obtained:

$$M_{\pm}=M_{1\pm}.M_{2\pm}, \tag{17}$$

The loading period or half-beat length can be approximated as follows:

$$L_\pi \approx \frac{\pi}{\Omega_1+\Omega_2}, \tag{18}$$

Thus, the length of one top silicon brick is $L_\pi$ and the top cladding layer alternates periodically throughout the propagation length. The simulation results revealed that for our structure, $|k_{xy}| \approx |k_{yx}|$ and $k_{xy} \approx k_{yx}^*$ ; where the imaginary parts were very small. Numerical, and analytical solutions of the coupled mode theory, equ. (12.a) and (8.b), give us almost the same results. From equ. (14) the preliminary value of the loading period before employing the numerical method to solve the coupled mode equation, equ. (12), was calculated.

In next section, first the band structure of the asymmetric loaded PC slab waveguide is calculated using PWEM. Therefore, frequency band over which the polarization rotator can be operated is determined.

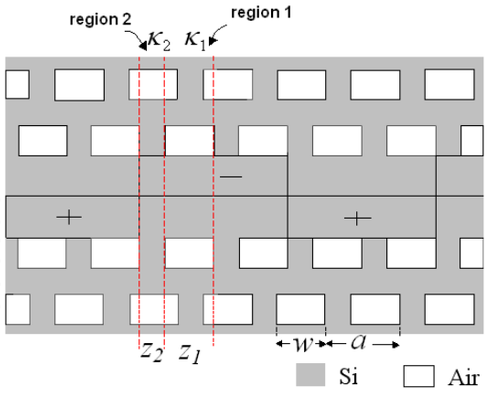


Fig. 5. Top view of the asymmetrically loaded PC based polarization rotator. The top cover layer is marked by the dark solid line in the figure. $\kappa_1$ and $\kappa_2$ represent the cross-coupling coefficient for regions 1 and 2 inside a unit cell.

### 3.3 Design of the polarization rotator

In this section the results of the design using both coupled mode theory and normal mode analysis are presented.

#### 3.3.1 Design of the polarization rotator using 3D-FDTD modal analysis

##### 3.3.1.1 PWEM analysis

The first step of the design of the polarization rotator structure is to calculate the frequency band over which lossless propagation takes place for both x-polarized and y-polarized waves and then proceed with the design using both normal mode analysis and coupled mode theory within the aforementioned frequency band. The asymmetric loaded PC slab waveguide shown in Fig. 3(b) was first simulated using PWEM to obtain the band diagram and the frequency band of the modes. The thickness of the PC slab structure plays an important role on the polarization dependent guiding (Bayat et al., 2007). It is possible to obtain maximum overlap between x-polarized and y-polarized waves by optimizing the thickness of the PC slab waveguide.The same design methodology was employed to design the thickness of the asymmetric loaded PC slab waveguide.

Fig. 6(a) shows the super-cell for the asymmetric loaded triangular PC slab waveguide. By including several unit cells in horizontal plane, the defect lines in the super-lattice structure are isolated. In PWEM analysis, the definition of the TE-like and TM-like waves is based on the symmetry planes of the modes. The dominant components of TM-like mode ($H_y$, $E_z$, $E_x$) and the non-dominant components ($E_y$, $H_z$, $H_x$) have even and odd symmetry w.r.t. y=0 plane, respectively. Similarly, the dominant components of TE-like mode ($E_y$, $H_z$, $H_x$) and the non-dominant components ($H_y$, $E_z$, $E_x$) have even and odd symmetry to y=0 plane, respectively. The thickness of the top loaded layer, $t_{up}$, is an important design parameter. Heuristically speaking, the larger the thickness of the upper layer is, the stronger the geometrical asymmetry is leading to a more compact device. However, to comply

with the fabrication constrains the upper limit of the thickness of the loaded layer is restricted to $t_{up}$=0.2a.

The band diagrams for two different slab thicknesses t=0.6a and t=0.8a are obtained by PWEM and plotted in Fig. 6(b) and (c), respectively. The thickness of the top loaded layer, width of the PC squares and refractive index of silicon are $t_{up}$=0.2a, w=0.6 and $n_{si}$=3.48, respectively. There are two modes depicted by dotted and solid lines. The mode graphed by dotted line resembles an index-guided mode except the mini-stop band observed at the zone boundary. We will call it index-guided mode. The other mode depicted by solid line will be called Bloch mode. The index-guided mode is considered to be y-polarized wave for which the dominant electric field component is in y-direction. On the other hand, the Bloch mode is considered x-polarized wave. For t=0.6a, the index-guided mode crosses the Bloch mode and is folded back at the zone boundary at a/λ=0.28. The Bloch mode touches the zone boundary (K) at a/λ=0.259 and crosses TE-like PC slab modes at a/λ=0.274. Since the index-guided mode and Bloch mode cross each other, the difference between the effective refractive indices of the two modes, which is proportional to $1/L_{\pi}$, varies with frequency significantly. Thus, the polarization converter made of a PC slab with t=0.6a is expected to be narrow band.

On the other hand, by increasing the thickness of the slab to t=0.8a, the index-guided mode has been pushed down to the lower frequencies. The index-guided mode depicted by dotted line in Fig. 6(c) has folded back at the zone boundary at a/λ=0.243. Within the frequency band of the Bloch mode, 0.257-0.267, the two bands are parallel; thus, the variation of the difference between the effective indices of the two modes and $L_{\pi}$ with frequency are negligible. In this diagram, the index-guided and Bloch modes also correspond to fast and slow modes, respectively. At normalized frequency of a/λ=0.267, Bloch mode crosses TE-like PC slab mode. In 3D-FDTD simulations, the central normalized frequency of a/λ=0.265 is assigned to f=600 GHz resulting in the unit cell size of a=132.5 μm. The cross-section of $E_x$, $E_y$, $H_x$ and $H_y$ components for TE-like input at a/λ=0.267 (f=604.5 GHz) are plotted in Fig. 7. Graphs verify the presence of PC slab modes. $E_y$ and $H_x$ components of PC slab modes own even symmetry w.r.t. y=0 plane as opposed to $E_x$ and $H_y$ components where have odd symmetry. Therefore, PC slab modes are TE-like verifying the PWEM analysis. Moreover, the field distribution inside the defect line indicates that $E_y$ and $H_x$ are the dominant components of electric and magnetic field, respectively indicating that TE-like wave at the input excites y-polarized wave. All four components of y-polarized mode have even symmetry with respect to y=0 and x=0 planes; although, the minor components of input wave, TE-like, ($E_x$ and $H_y$) have odd symmetry w.r.t y=0 plane. Thus, TE-like input wave has been evolved into the mode of the asymmetric loaded PC slab waveguide. By further increasing the thickness of PC slab waveguide, higher order modes will be pushed down inside the bandgap; which is not suitable for our application. Having compared the band diagram for t=0.6a and t=0.8a; it is seen that t=0.8a suits better for the polarization conversion application.

Now that the overlap between x-polarized and y-polarized guiding are defined, 3D-FDTD simulation for extracting the modal characteristics of asymmetric loaded PC slab waveguide will be limited to the aforementioned frequency band. In following, the modal analysis using 3D-FDTD simulation is presented.

(a)

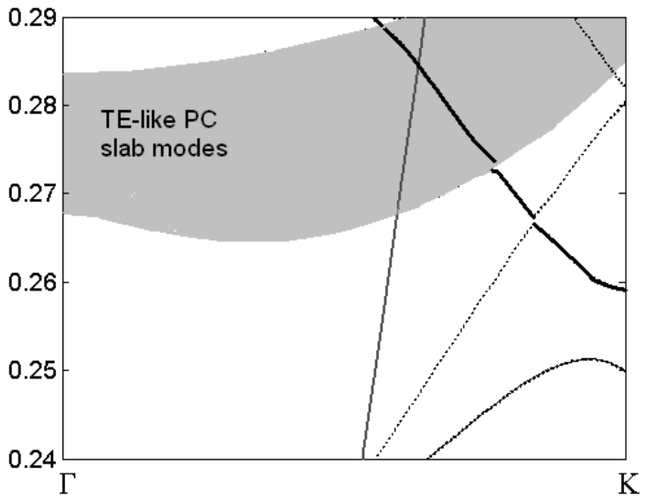


(b)

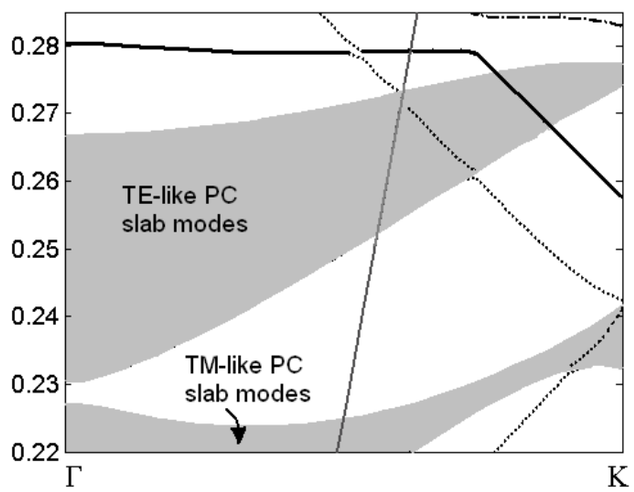


(c)

Fig. 6. (a) The supercell of the asymmetric loaded PC slab waveguide for PWEM analysis. The band diagram for the asymmetric loaded PC slab waveguide obtained by PWEM for (b) t=0.6a, $t_{up}$=0.2a and w=0.6a (c) t=0.8a, $t_{up}$=0.2a and w=0.6a.

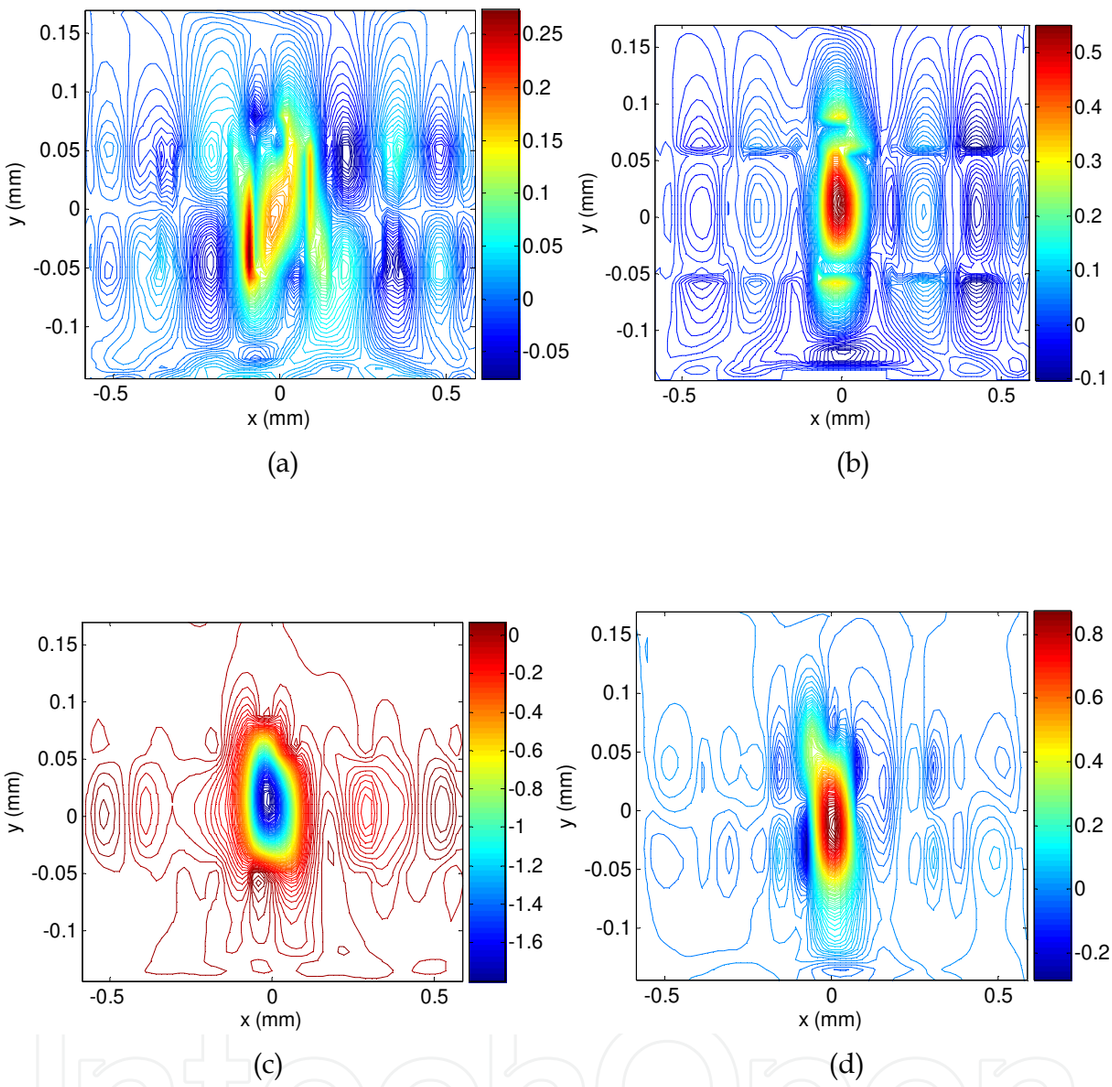


Fig. 7. Cross-section of electromagnetic field components obtained by 3D-FDTD analysis of asymmetric loaded PC slab waveguide at f=604.5 GHz (a/λ=0.267) with t=0.8a, w=0.6a, $t_{up}$=0.2a, $n_{si}$=3.48 (a) $E_x$ (b) $E_y$ (c) $H_x$ (d) $H_y$.

#### 3.3.1.2 3D-FDTD modal analysis

To calculate birefringence and $L_\pi$, it is required to obtain the vector-propagation characteristics of normal modes of the asymmetric loaded PC slab waveguide, Fig. 3(b), using 3D-FDTD simulation. To calculate the birefringence of the structure, the effective frequency-dependent indices of refraction of the structure for both $E_x$ and $E_y$ components are calculated using SFT analysis of transverse electric field components along the propagation direction at the center point of the defect line (x=0, y=0). For 3D-FDTD simulation, the input is a single frequency sinusoidal with guassian distribution in space. As

time proceeds and wave propagates along z-direction inside the defect line, the wave evolves into the modes of the structure. Thus, in the steady state case by applying SFT to the field distribution along the propagation direction at any point inside the defect line, the propagation characteristics of the modes can be obtained.

In our design example, the structural parameters of the PC polarization rotator are determined by assigning the normalized central frequency of the fundamental mode, 0.265, to the operating frequency. For example for f=600 GHz corresponding to the normalized frequency of 0.265, the unit cell size would be 132.5 μm (a= 0.265λ). Fig. 6 (c) shows that the overlap between x-polarized and y-polarized guiding lay within the frequency band of 0.258-0.267. The normalized SFT diagram for the input normalized frequency of a/λ=0.265 is calculated and plotted in Fig. 8. Fig. 8(a) and 8(b) correspond to TE-like and TM-like excitations, respectively. For TE-like excitation, at the input $E_y$ is the dominant component; however, as the wave proceeds, the input evolves into the normal modes of structure that are depicted by the two dominant peaks in SFT spectrum. In SFT spectrum, the horizontal axis is the $1/\lambda_g$ where $\lambda_g = \frac{\lambda}{n_{eff}}$ . λ and $n_{eff}$ are free space wavelength and effective refractive index of the propagating mode, respectively. For example, in Fig. 8(a) the SFT spectrum of $E_y$ has a peak at $1/\lambda_g$=5.16 where coincides with one the peaks of SFT spectrum of $E_x$ component. The corresponding effective refractive index $n_{eff}$ or $n_f$ (refractive index of fast normal mode) would be 2.58. The other peak of SFT spectrum of $E_x$ component correspond to x-polarized or slow mode. It has been located at $1/\lambda_g$=5.52 resulting in $n_{eff}$ or $n_s$ (refractive index of slow normal mode) of 2.76. It is seen that the asymmetric loaded layer has induced a large birefringence. Having determined the effective refractive indices of the two normal modes, the half-beat length or $L_\pi$ can be calculated using equ. (1). For the two refractive indices calculated above at λ=500 μm, half-beat length ($L_\pi$) would be 1.39 mm which is equivalent to 10.5a, a is the unit cell of PC slab. The same values are obtained for $n_f$ and $n_s$ from graph 7(b) which is plotted for TM-like input wave.

Another important parameter that can be extracted from modal analysis is polarization rotation angel, $\varphi$; which is tilted angel of optical axes with respect to Cartesian coordinate. The following expression is used to calculate the polarization rotation angel:

$$\varphi = \tan^{-1}\left(\frac{abs(SFT(E_x))}{abs(SFT(E_y))}\right)\Big|_{@\,peak,TE-like} = \tan^{-1}\left(\frac{abs(SFT(E_y))}{abs(SFT(E_x))}\right)\Big|_{@\,peak,TM-like} \quad (19)$$

Value of polarization rotation angel ($\varphi$) for above example is 6.5°. Polarization rotation angel is important in determining the total number of loaded layers required to achieve 90° polarization rotation. For this example, at the end of fourth loaded layer, the polarization of input wave should be rotated by 104° that exceeds 90°. To compensate the extra rotation angel, the length of the last top loaded layer can be increased. Thus, the normal mode analysis provides with the length and total numbers of top loaded layers.

Below normalized frequency of a/λ=0.257, only y-polarized wave is guided; thus, no polarization rotation is expected as x-polarized wave is not guided. To verify it, normalized SFT diagram of asymmetric loaded PC slab waveguide for the input normalized frequency

of a/λ=0.252 is calculated and plotted in Fig. 9. The input wave is y-polarized or TE-like wave. Thus, the dominant component of electric field is $E_y$. The normalized SFT spectrum of both $E_y$ and $E_x$ components of electric field are plotted in Fig. 9. The SFT diagram of $E_x$ has only one peak verifying PWEM diagram that only y-polarized wave is guided at this frequency.

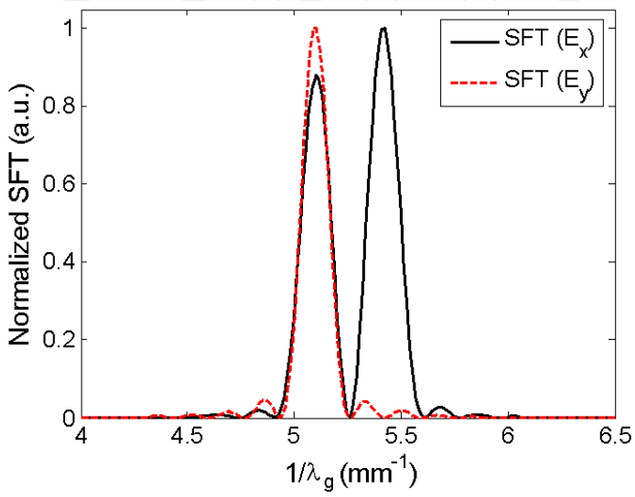


(a)

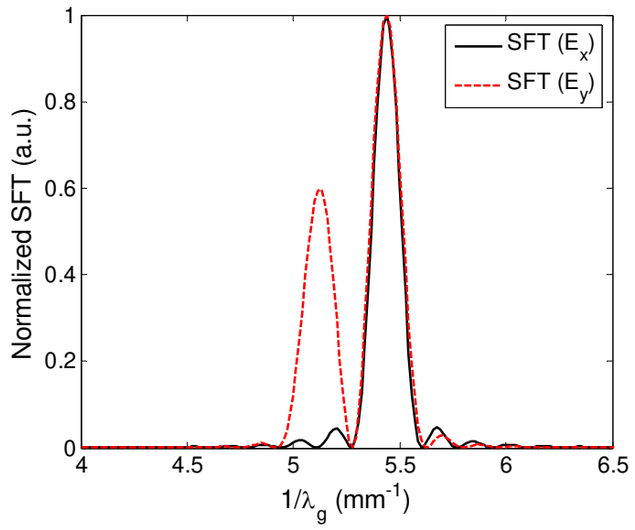


(b)

Fig. 8. The normalized SFT spectrum of transverse electric field components of asymmetric loaded PC slab waveguide for (a) TE-like wave input and (b) TM-like wave input (w=0.6a, t=0.8a and $t_{up}$=0.2a, λ=500 μm).

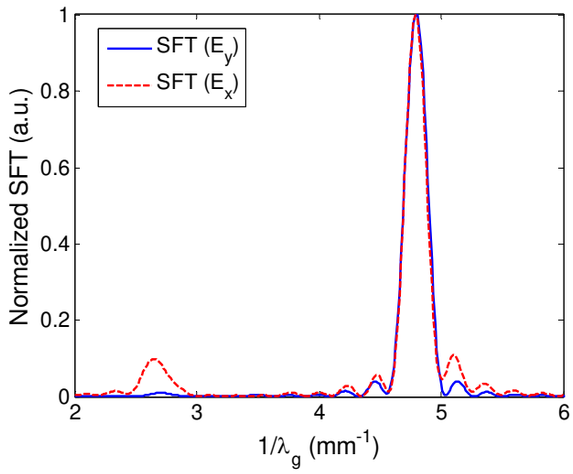


Fig. 9. The normalized SFT spectrum of transverse electric field components of asymmetric loaded PC slab waveguide for TE-like wave input (w=0.6a, t=0.8a and $t_{up}$=0.2a, a/$\lambda_0$=0.252).

In next section, the design of the polarization rotator using coupled-mode theory based on semi-vectorial modes is presented.

**3.3.1.3 Design of the polarization rotator using coupled-mode theory**

In this section, coupled mode theory discussed earlier was employed to design the asymmetrically loaded PC polarization rotator. In order to employ the coupled mode theory, first the semi-vectorial modes of the asymmetrically loaded PC slab waveguide, Fig. 3(b), must be calculated. Semi-vectorial BPM was employed for semi-vectorial modal analysis of the structure. The normalized electric field for x-polarized (TM-like) and y-polarized (TE-like) waves for the normalized frequency of a/λ=0.265 are shown in Fig. 10(a) and 10(b), respectively. It shows that the electric field distribution is asymmetric in both vertical and lateral directions as a result of the geometrical asymmetry. The propagation constants of the corresponding modes were calculated using semi-vectorial BPM simulation, as well. The effective refractive indices of x-polarized and y-polarized waves were 2.6567 and 2.5007, respectively. A big birefringence was observed as expected in PC slab waveguide structure. For aforementioned parameters, the coupling coefficients of the periodic asymmetric loaded PC polarization rotator (shown in Fig. 3(b)) were calculated using equ. (13) for both regions of 1 and 2, depicted in Fig. 5. Using equ. (15), the loading period was calculated, 10.8a. The value of half-beat length, $L_\pi$, computed using coupled-mode theory and normal mode analysis were 10.8a and 10.5a, respectively. Thus, both methods deliver the same results that is a proof of the effectiveness of them. Fig. 11 shows the power exchange between the two polarizations along the propagation distance for a/λ=0.275, 0.265 and 0.255, $\lambda_0$=500 μm (600GHz). The length of each top loaded layer is 10a.

Defining the power conversion efficiency (P.C.E.) as following:

$$P.C.E. = \frac{P_{TM}}{P_{TM} + P_{TE}} \times 100 = \frac{a_x^2}{a_x^2 + a_y^2} \times 100 \tag{20}$$

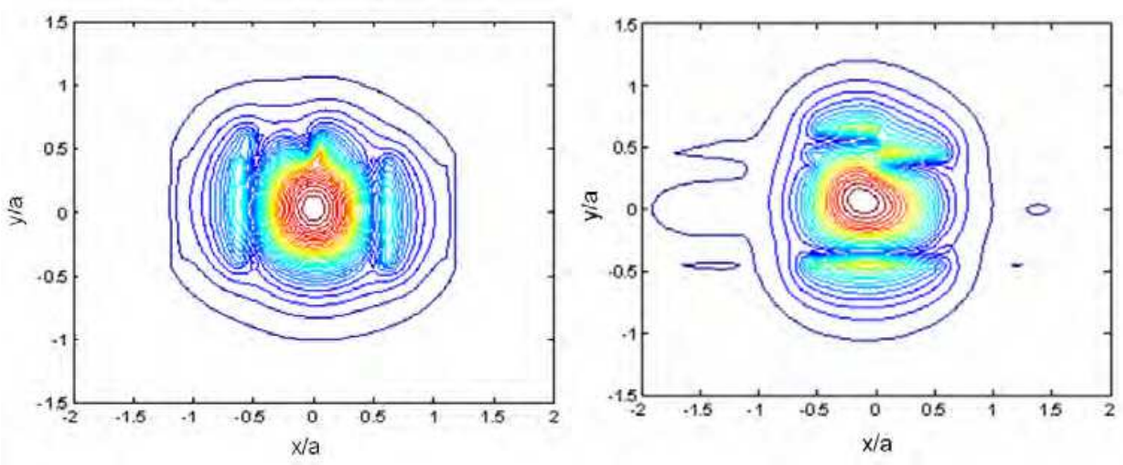


(a) (b)

Fig. 10. The profile of (a) $E_x$ and (b)$E_y$ components of x-polarized and y-polarized modes of the structure shown in Fig. 3(b) obtained by semi-vectorial 3D BPM analysis ($t=0.8a$, $t_{up}=0.2a$, $w=0.6a$, $a=132.5$ μm, $n_{si}=3.48$ and $\lambda=500$ μm).

For $a/\lambda=0.265$ ($\lambda=0.5$ mm), 96% efficiency at z=7.2 mm (millimeter) was achieved. It is expected that by increasing or decreasing the normalized frequency, the power conversion efficiency reduce. To achieve high power conversion efficiency, the last silicon brick (top loaded layer) was no flipped around z-axis. In other word, the length of the last silicon brick was larger than 10a as it was predicted by normal mode analysis method, as well. The P.C.E. for $a/\lambda=0.275$ and 0.255 is larger than 75% at z=7.2 mm. Thus, it is expected to have a very high P.C.E. within the frequency band of the defect mode (0.258-0.267).

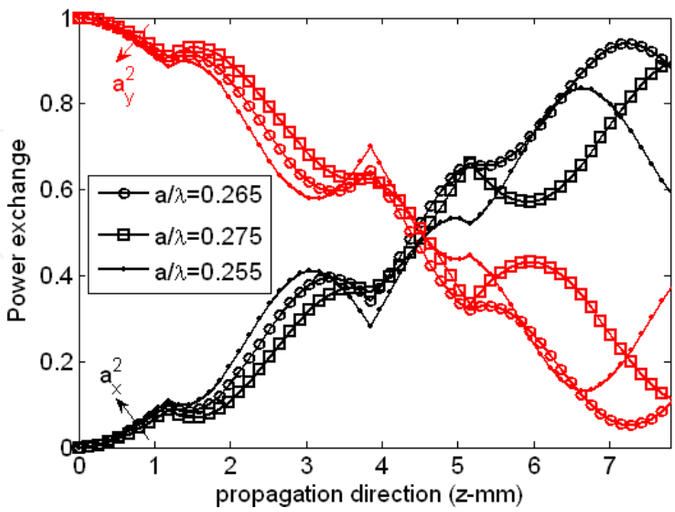


Fig. 11. Power exchange between the x-polarized and y-polarized wave versus the propagation length ($t=0.8a$, $t_{up}=0.2a$, $w=0.6a$, $a=132.5$ μm, $n_{si}=3.48$) for $a/\lambda=0.255$, 0.265 and 0.275 obtained by coupled-mode analysis.

### 3.4 3D-FDTD simulation of polarization rotator structure

Both Design methodologies suggest that high power exchange rate is expected to be observed within the frequency band of 0.258-0.267, the overlap frequency band between the fast and slow mode guiding. To verify the aforementioned results, 3D-FDTD was employed to simulate the polarization rotator. The simulated structure (Fig. 3(a)) consists of 70 rows of holes along the propagation direction (z-direction) and 11 rows of holes (including the defect row) in x-direction. The mesh sizes along the x, y and z-directions (Δx, Δy and Δz) are Δx=Δz=0.0331λ and Δy=0.0172λ. The perfectly matched layer (PML) boundary condition was applied for all three directions. Time waveforms in 3D_FDTD were chosen as a single frequency sinusoid. The spatial distribution of the incident field was Guassian. The frequency of the input signal lies within the frequency band of the defect mode (0.258-0.267 corresponding to 586-601 GHz). As the wave proceeds, the polarization of the input signal starts rotating. The power exchange between ($E_x$, $E_y$) and ($H_x$, $H_y$) components was observed. To achieve the maximum power conversion, the size of the last top silicon brick was 15a instead of 10a. Fig. 12 shows the contour plot of transverse field components, $E_x$, $E_y$, $H_x$ and $H_y$ at the input for a/λ=0.265. The input excitation is TE-like; $E_y$ and $H_x$ are the dominant components and have even parity as opposed to the non-dominant components $E_x$ and $H_y$ that have odd symmetry with respect to y=0 plane.

As the wave proceeds, the power exchange is observed between ($E_y$, $E_x$) and ($H_x$, $H_y$) components. The contour plot of $E_x$ and $H_y$ at a point close to the output are plotted in Fig. 13. It is seen that the parity of the $E_x$ and $H_y$ components have changed and become the dominant component. The amplitudes of $E_y$ and $H_x$ have been decreased more than an order of magnitude and reached to zero at the output plane. Thus, 90° rotation of polarization is realized at the output.

To show the power exchange between the two polarizations, the z-varying square amplitudes of $E_x$ and $E_y$ components were graphed. Fig. 14 shows $a_x^2(z)$ and $a_y^2(z)$ along the propagation direction for the normalized frequency of 0.265 corresponding to the free space wavelength of 500 μm. The two main elements contributing to the numerical noise are local reflections and imperfections of absorbing layer. Dots in the figure are the actual values of 3D-FDTD analysis. To have a smooth picture of $a_x^2(z)$ and $a_y^2(z)$ variations along the propagation direction, a polynomial fit to the data using least square method is also shown in the figure. Each plot consists of more than 100 data points. The FDTD "turn-on" transition of the input wave has also been included in the graph (first 0.5 mm). This portion is obviously a numerical artifact of the FDTD scheme. After almost 6 mm (12λ), the complete exchange, as can be seen in the Fig. 14, has taken place. Comparing this graph with coupled-mode (counterpart plot in Fig. 11), it is seen that the power exchange between the two polarizations takes place at smaller propagation distance; 6 mm in comparison with 7.2 mm. Moreover, the value of P.C.E obtained by 3D-FDTD is close to 100 %; whereas, P.C.E for the same wavelength for coupled-mode analysis is 96%. On the other hand, normal mode analysis method predicted that 100% polarization conversion could take place at less than $4.5L_{\pi}$, 6 mm. Therefore, normal mode analysis design methodology provides more accurate results.

3D-FDTD simulations were repeated for other frequencies to obtain the frequency dependence of polarization conversion. The power exchange rate for both coupled-mode analysis and 3D-FDTD are graphed versus the normalized frequency in Fig. 15. Coupled-mode analysis shows that P.C.E of higher than 90% is achieved within the normalized

frequency band of 0.258-0.267. 3D-FDTD simulation results show that the P.C.E higher than 90% is realized within the frequency band of 0.258-0.267; over which the defect mode lies.

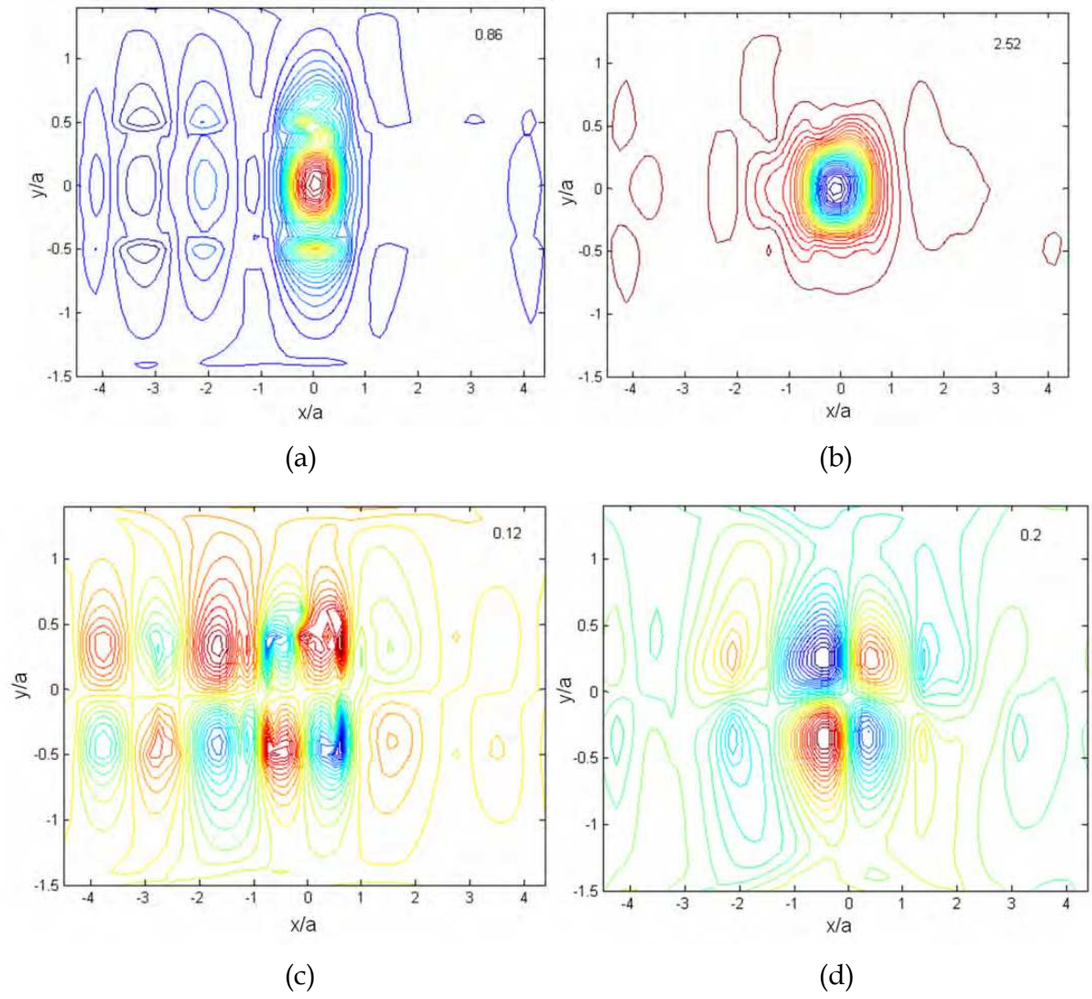


Fig. 12. The contour plot of the cross section of (a) $E_y$, (b) $H_x$, (c) $E_x$ and (d) $H_y$ components at the input plane (t=0.8a, $t_{up}$=0.2a, $n_{si}$=3.48, a/λ=0.265, λ=500 μm).

At normalized frequencies higher than 0.267, *Ey* starts leaking energy to the TE-like PC slab modes as it crosses the TE-like PC slab modes, Fig. 6(c). For example, FDTD simulation of the power exchange between x-polarized and y-polarized waves for a/λ=0.275 is graphed in Fig. 16. It is seen that for a/λ=0.275, the slope of the drop of $a_y^2(z)$ is much sharper than the slope of the rise of $a_x^2(z)$. More importantly, $a_y^2(z)$ is dropping much faster than that of a/λ=0.265, Fig. 14. This observation can be interpreted as if $E_y$ is dissipating and leaking energy into the TE-like slab modes. Thus, a sudden drop on power exchange rate is observed at normalized frequencies higher than 0.267. Semi-vectorial BPM analysis utilized for modal analysis is not capable of including the PC modes; thus, in power exchange graph calculated by coupled-mode analysis for normalized frequency of a/λ=0.275 (Fig. 11), no power dissipation is observed as opposed to 3D-FDTD simulation (Fig. 16).

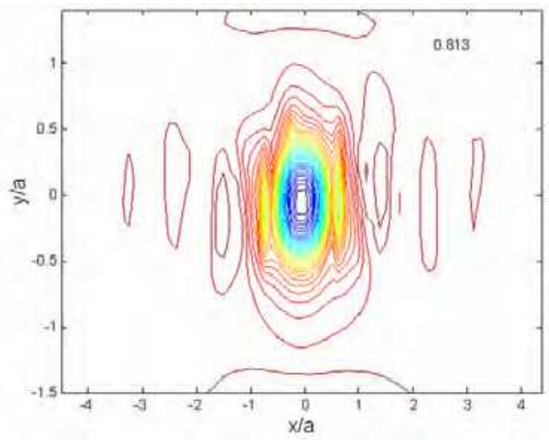


(a)

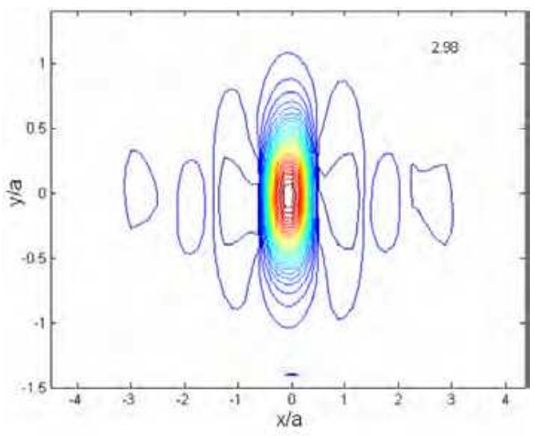


(b)

Fig. 13. Contour plot of the cross section of (a) $E_x$ and (b) $H_y$ at z=5.5 mm (t=0.8a, $t_{up}$=0.2a, $n_{si}$=3.48, a/λ=0.265, λ=500 μm).

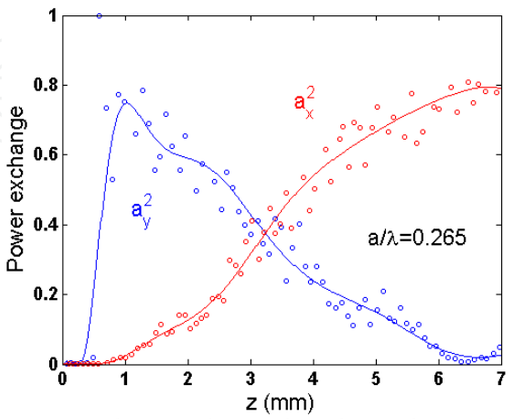


Fig. 14. Power exchange between the x-polarized and y-polarized wave versus the propagation length for a/λ=0.265 obtained by 3D-FDTD simulation (t=0.8a, $t_{up}$=0.2a, w=0.6a, a=132.5 μm, $n_{si}$=3.48, λ=500 μm).

At frequencies lower than a/λ<0.255, only y-polarized wave is guided; thus, no power exchange between the two polarization takes place. Our recommendation is to avoid this region for the design of the polarization rotator. Having compared FDTD and coupled-mode analyses, coupled-mode theory approach is effective within the frequency band where x-polarized and y-polarized guiding overlap. The other approach described in 3.3.1.2 can predict the frequency response of the PC based polarization rotator. In polarization rotation angel graph versus frequency obtained using normal mode analysis, a sudden jump in the polarization rotation angel at normalized frequencies larger than 0.268 and smaller than 0.257 is observed that is a sign of changing the behavior of the modes; hence the polarization rotator.

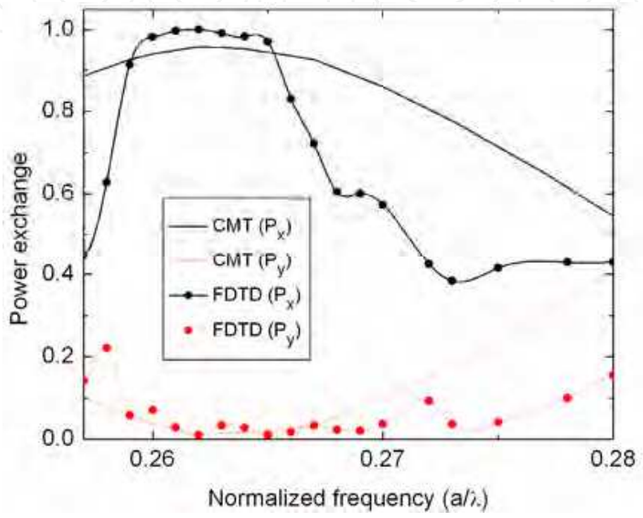


Fig. 15. Power exchange between the x-polarized and y-polarized waves versus frequency for both coupled-mode analysis and 3D-FDTD simulations ((t=0.8a, $t_{up}$=0.2a, w=0.6a, a=132.5 μm, $n_{si}$=3.48).

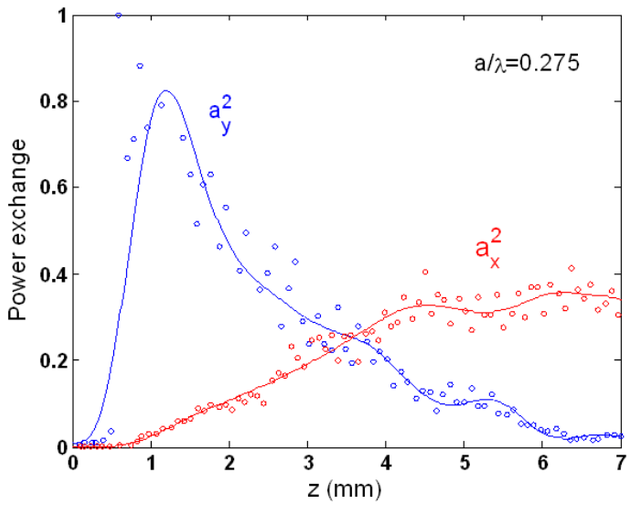


Fig. 16. Power exchange between the x-polarized and y-polarized wave versus the propagation length for a/λ=0.275 obtained by 3D-FDTD simulation (t=0.8a, $t_{up}$=0.2a, w=0.6a, a=132.5 μm, $n_{si}$=3.48, λ=500 μm).

## 4. Fabrication technique

In this section, the fabrication process of the Si membrane PC technology for THz application is presented. Highly resistive silicon (> 5-10 kΩ-cm) was employed to implement PC based membrane structures for THz applications. Here, a novel PC technology for the THz wave that is a potential candidate as a compact and low loss media for THz wave propagation was introduced. More importantly, this technology has a potential for integration with other optoelectronic and micro-electronic devices. Devices were fabricated in the frequency band of 200 GHz - 1 THz. The thickness of the device layer is chosen between 80 µm and 400 µm based on the design. The thickness of the buried oxide layer that separates the silicon device layer from the silicon handle layer could be varied between 0.5 µm-5 µm. Handle silicon layer is a low resistive silicon that attenuates the THz signal significantly and must be taken into consideration in the fabrication technology design.

The fabrication process consists of both front side and backside processing of the SOI wafer. The front side processing involves etching of deep holes into the silicon layer. Backside processing consists of opening window at the backside of the devices to prevent coupling of the THz wave to the lossy substrate modes and guarantee low loss propagation. To pattern the device layer, standard lithography is utilized as opposed to the optical PC structure that requires nanometer range lithography. In order to etch deep holes (> 100 µm), Deep Reactive Ion Etching (DRIE) is required. Thick photoresist must be utilized for photolithography to stand the long etching process. 4 µm thick photoresist (S1827) was employed as a soft mask for the DRIE process.

The etching of the holes was carried out using an optimized DRIE process to create holes with smooth vertical side walls and the desired aspect ratio. The Bosch process which alternated between two modes of nearly isotropic plasma etching using $SF_6$ for 7 sec and deposition of chemically inert passivation layer using $C_2F_8$ for 2 sec was employed. The $SF_6$ and $C_2F_8$ flow rates were 300 sccm and 150 sccm, respectively. The process temperature is kept at 20$^o$C. The etching rate is around 5µm/min, and can vary slightly during the etching process. Buried oxide acts as an etch stop.

The second phase of the process is opening a window at the backsides of the SOI wafer to construct the membrane PC structure. Handle silicon is a thick silicon (525 µm), which was removed by wet chemical etching. 30% KOH etching at 90$^o$C, which gave an etching rate of almost 50µm/hr, was used. The front side of the wafer must be protected from the KOH etching. The KOH etching was carried out by a custom made wet etching tool which only exposes the backside of the wafer to hot KOH solution. KOH mask that covers the unetched areas must withstand 10 hours of KOH at 90$^o$C. A thick amorphous silicon nitride film (a-SiN) of 1µm, was deposited using PECVD technique to function as the hard mask at the backside of the SOI wafer. The second lithographic step was performed to pattern the SiN layer for the opening windows at the backside of the SOI wafer. Again buried silicon dioxide functions as the etching stop (Bayat et al., 2009).

The SEM image of a fabricated membrane PC slab waveguide is shown in Fig. 17 (a). It shows that the window under the active area (waveguide area) has been etched nicely. Fig. 17 (b), is SEM picture of the top side showing the air holes close-up. It can be seen that the walls are sharply etched. The backside etching is also very important and critical. Fig. 17 (c)

shows the SEM picture of the backside. It can be seen that the back is etched uniformly; the oxide at the back can be easily removed by buffered HF (BHF).

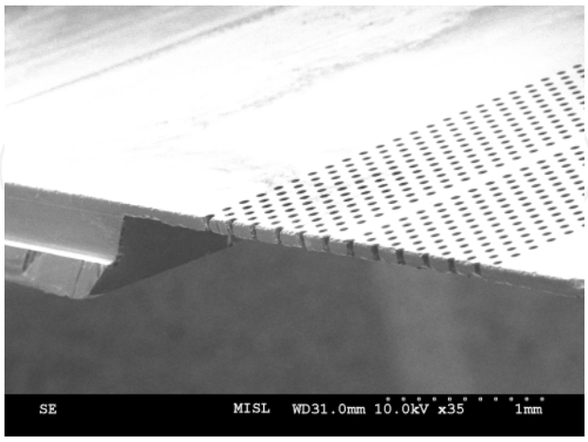


(a)

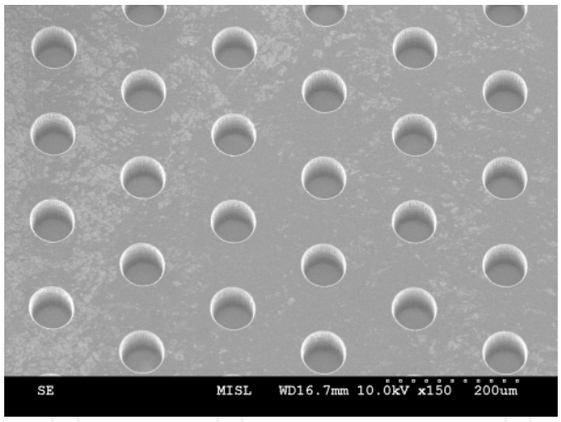


(b)

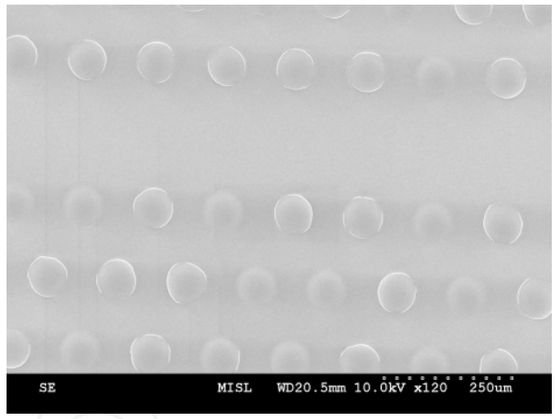


(c)

Fig. 17. SEM picture of fabricated (a) PC membrane slab waveguide (b) front side and backside of the PC structure.

Polarization rotation devices for potential applications in the THz frequency band (200 GHz – 1THz) were fabricated. The fabrication of this PC based polarization rotator is more complex in a sense that the front side processing requires two sets of masks. The first mask is employed to create the periodic loading layers. The second mask is for patterning of the PC slab waveguide. The third mask is used to open window at the back side of the structure. Fig. 18(a) shows the SEM picture of the periodic asymmetric loaded PC slab waveguide with square holes. The SEM picture shows that the walls are very sharp. In Fig. 18(b), the SEM picture of the periodic asymmetric loaded PC slab waveguide for circular air holes pattern is presented.

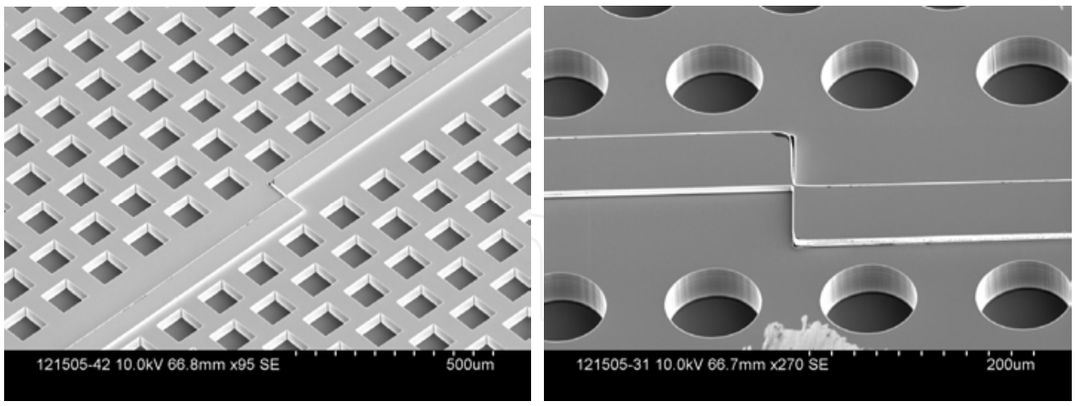


(a) (b)

Fig. 18. SEM picture of (a) square hole PC polarization converter (b) circular hole PC and circular hole polarization converter.

## 5. Characterization setup

Series of devices in the frequency range of 0.2-1 THz are fabricated. The devices are being prepared to be characterized using Agilent Millimeter-wave PNA-X network analyzer (up to 500 GHz). The characterization setup is simulated using HFSS v.11 and SEMCAD (Bayat et al., 2010). In this section, full HFSS simulation results are presented that are considered strong validations of expected measurement outcomes. In the new setup, sub-mm metallic waveguides are employed as the interface between the PNA coaxial cables and input/output (I/O) tapers of the PC-slab waveguide devices. For example for central frequency of 200 GHz, WR-5 is utilized with size of 0.0510″ × 0.0255″ (1.295mm × 0.647mm). The total thickness of the polarization rotator assuming that 200 GHz corresponds to normalized frequency of $a/\lambda=0.263$ would be 0.0155″ (0.395 mm); thus, there is a good match between WR-5 and input taper. A single-defect line PC slab waveguide is employed as the calibration reference. The waveguide is designed to guide both TE-like and TM-like wave (Bayat, et al., 2007).

Fig. 19(a) shows the sketch of the setup designed to couple electromagnetic wave in and out of the waveguide utilizing sub-mm metallic waveguides. To couple the electromagnetic wave to the defect line, a taper structure is utilized as shown in Fig. 19(a). The geometry of the I/O tapers must be designed properly to maximize the coupling efficiency to the defect line of PC slab waveguide.

In HFSS (v.11) simulations, the input wave is TE10 mode of the rectangular transition waveguide that has been polarized along y direction. The structural parameters of the PC slab waveguide are as follows: $w=0.6a$, $t=0.8a$, $a=0.378$ mm, $n_{si}=3.48$ and $\tan\delta=1\times10^{-4}$; where a, w, t, $n_{si}$, $\tan\delta$ are the unit cell, width of square holes, thickness of the PC slab waveguide, refractive index and loss tangent of silicon, respectively. The central frequency is set to 200 GHz corresponding to the normalized frequency of $a/\lambda=0.252$. The power transmission takes place through the PC defect line. The frequency response of the setup is plotted in Fig.

19(b). $S_{11}$ (reflection) and $S_{21}$ (transmission) are depicted by dashed and solid lines, respectively. The graphs show that the insertion loss is less than 2 dB in the entire band from 190 to 210 GHz. The return loss is higher than 20 dB. Thus, the waveguide can be employed as a wide band low loss transmission line.

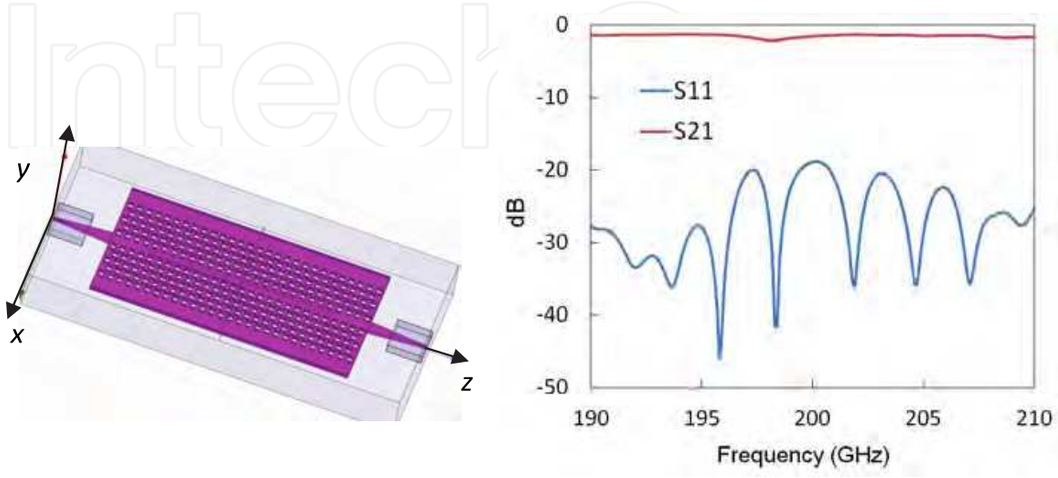


(a) (b)

Fig. 19. (a) The schematic of the characterization setup consisting of PC slab waveguide, input/output tapers and rectangular waveguides (b) $S_{11}$(blue line)-$S_{21}$(red line) (return loss-insertion loss) plots of the PC slab waveguide

The same setup as in Fig. 19(a) has been used to characterize the polarization rotator. The input wave is TE10 mode with electric field pointing in y direction ($E_y$). For 90$^o$ polarization rotator, the input polarization rotates by 90$^o$ so that at the output plane the x-component of electric field is dominant. The output rectangular metallic waveguide is to be rotated by 90$^o$ to support $E_x$ field. Fig. 20(a) shows the schematic of the polarization rotator with two alternating top loaded layers. Previously, it was shown that for this design the rotation angle for each top loaded layer is 6.5$^o$; therefore, the polarization rotator with two top loaded layers rotates the input polarization by an angle of $2^2$*6.5$^o$=26$^o$. In this design, normalized frequency of a/λ=0.263 (where a and λ are the unit cell size and free space wavelength) is assigned to 200 GHz; thus, it is expected to see approximately 26$^o$ polarization rotation in the frequency band of 196-204 GHz corresponding to normalized frequency band of a/λ=0.258-0.267.

If the output taper shown in Fig. 19(a) was placed at the output, $E_x$ component of the field would have been exposed to the geometry variation of the output taper imposing reversed rotation; the width of the taper in x-direction is decreasing along the propagation. To improve the polarization extinction ratio and enhance the coupling of $E_x$ component to the rectangular metallic waveguide, the output taper was rotated by 90$^o$, shown in Fig. 20 (a). Having rotated the output waveguide, it supports only $E_x$ component and $E_y$ component of the field reflects back. Thus, $S_{21}$ and $S_{11}$ parameters would provide a good measure of the polarization extinction ratio.

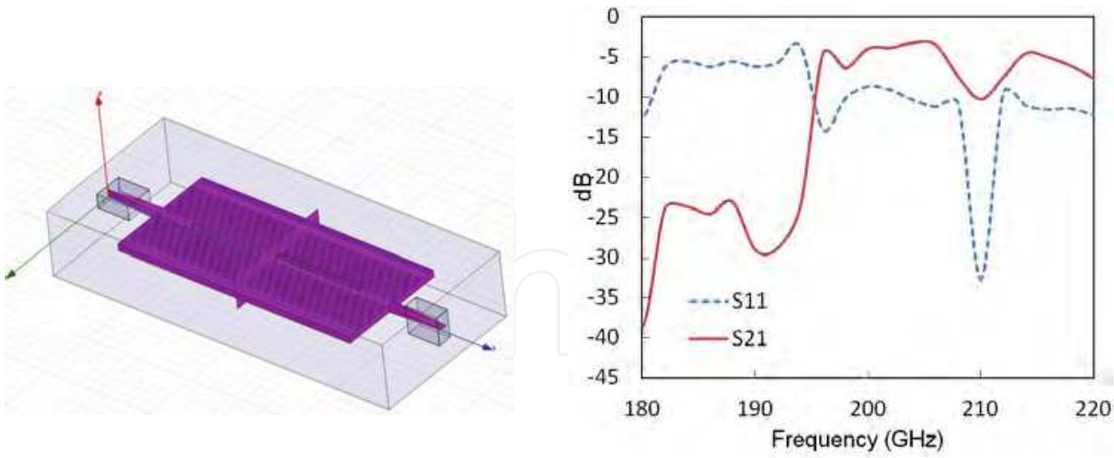


(a) (b)

Fig. 20. (a) The schematic of the polarization rotator with the rotation angle of 26° with input/output tapers and waveguides (b) $S_{11}$ (blue dashed line) and $S_{21}$ (solid red line) plots of the structure.

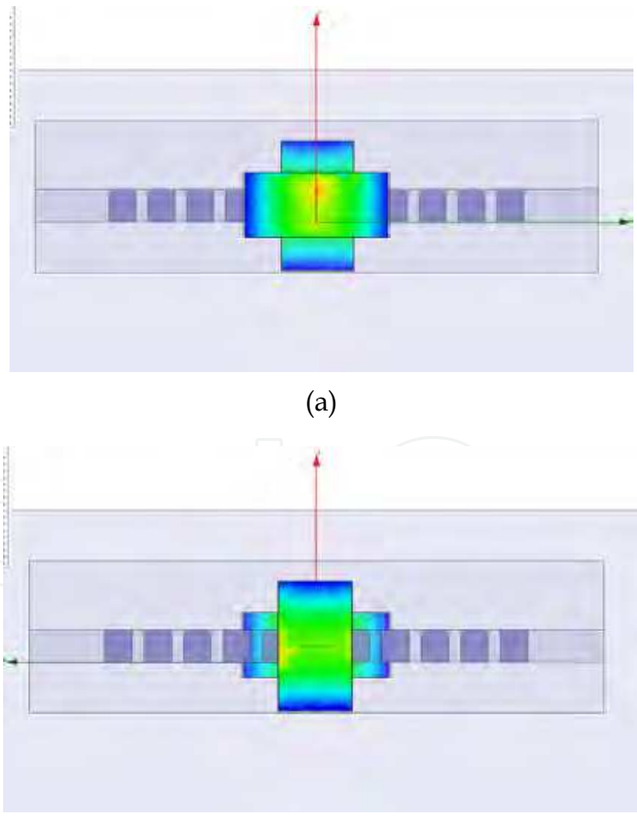

(a)

(b)

Fig. 21. Field distribution at the (a) input, and (b) output ports of the polarization rotator at 200 GHz.

Fig. 20(b) shows $S_{11}$ and $S_{21}$ plots from the HFSS simulations. It shows that within the frequency band of 196-206 GHz, $S_{21}$ is higher than -4 dB and $S_{11}$ is less than -10 dB. The bandwidth is in a good agreement with the design results presented in Sec. 3. The electric field distribution at the input and output ports are shown in Fig. 21. The input and output electric fields are laid out in x and y-direction, respectively. The electric field distribution clearly pictures the electric field rotation.

The structure shown in Fig. 22(a) is designed to rotate the input polarization by 90°. The 4.5 top loaded layers provide 90° rotation. The output taper has not been rotated 90° because of the fabrication limits and feasibility issues of such taper. Thus, we would expect to observe lower coupling efficiency of $E_x$ component to the output rectangular waveguide. Due to the computational limits of HFSS, SEMCAD was employed to simulate the structure using 3D-FDTD method.

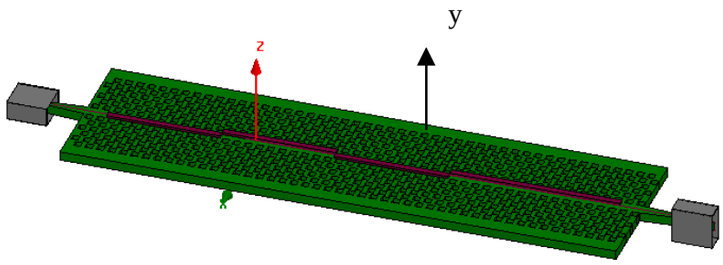


(a)

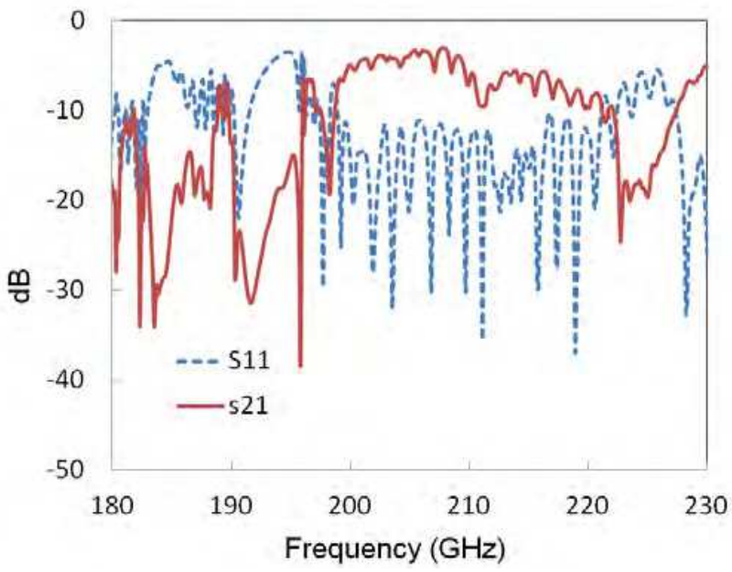


(b)

Fig. 22. (a) Schematic of the polarization rotator with an angle of rotation of 90° (b) $S_{11}$ (blue dashed line) and $S_{21}$ (solid red line) plots.

Fig. 22(b) shows the spectrum of S-parameters. It is very similar to S-parameters graph presented in Fig. 20(b). In Fig. 22(b), within the frequency band of 199-208 GHz, $S_{21}$ and $S_{11}$ are higher and less than -5 dB and -15 dB, respectively. Since the structure was designed for 90° rotation, higher polarization extinction ratio was expected in comparison with the polarization rotator with 26° angle of rotation. The S-parameter plot in Fig. 22(b) has large fluctuation and it is not as smooth as the S-parameter shown in Fig. 20(b). These fluctuations are due to the numerical noise of 3D-FDTD analysis.

Snap shots of Ex and Ey components at f=205 GHz is presented in Fig. 23. Fig. 23(a) shows that the TE10 mode has launched $E_y$ –fields in the left side and it is well-confined inside the input taper and then couples into the defect line of the PC slab waveguide. On the other hand, $E_x$–field component in Fig. 23(b) is weak at the left (input) side of the defect line; the color bar shows that it is one order of magnitude smaller than $E_y$ component. As $E_y$ –field mode propagates inside the defect line of PC slab waveguide based polarization rotator, it gradually rotates and converts to $E_x$ component. At the other end of the PC slab waveguide, $E_x$ component seems to be one order of magnitude larger than $E_y$. At the output taper, $E_x$ will expose to the geometry variation of the taper resulting in reverse polarization conversion. Thus, the polarization conversion efficiency would decrease.

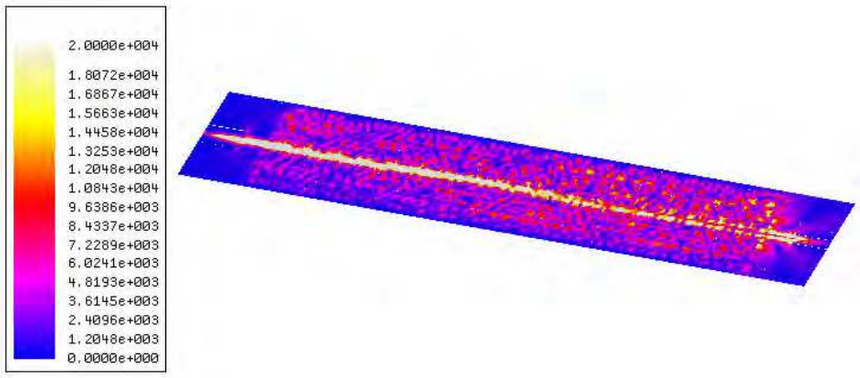


(a)

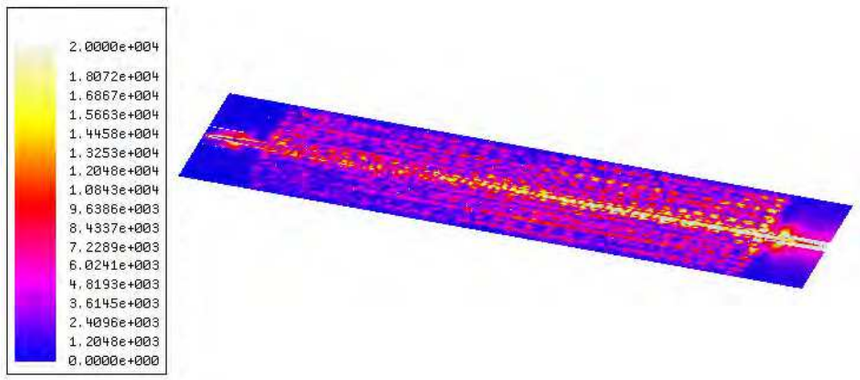


(b)

Fig. 23. Snap shots of (a) $E_y$ and (b) $E_x$ componnets obtained using 3D-FDTD analysis.

## 6. Conclusions

The focus of this chapter was on design and fabrication of PC slab waveguide based polarization processor devices. A summary of the key achievements are highlighted as following:

- A novel compact PC slab waveguide based polarization rotator was introduced and designed. PC based coupled-mode theory was developed to design the structure. Coupled-mode theory provides with a simple yet closed form method for initial design. Square-hole PC was preferred in order for simplicity of the closed-form formulations. The design was refined using rigorous electromagnetic numerical method (3D-FDTD). 3D-FDTD simulation results verified the robustness of coupled-mode theory for design and analysis of PC based polarization rotator.
- To extend the design to more general shape PC based polarization rotator, a design methodology based on vector-propagation characteristics of normal modes of asymmetric loaded PC slab waveguide was introduced. The vector-propagation characteristics of normal modes of the structure were calculated utilizing 3D-FDTD method combined with SFT. Profile and propagation constants of slow and fast modes of asymmetric loaded PC slab waveguide were extracted from 3D-FDTD simulation results. The half-beat length, which is the length of each loaded layer, and total number of the loaded layers are calculated using aforementioned data. This method provides with exact values of the parameters of the polarization rotator structure.
- SOI based PC membrane technology for THz application was developed. PC slab waveguide and polarization rotators were fabricated and characterized employing this technology.

## 7. References


Barwicz, T. & Watts, M.R. & Popović, M.A. & Rakich, P.T. & Socci, L. & Kärtner, F.X. & Ippen, E.P. & Smith, H.I. (2007) *Polarization-transparent microphotonic devices in the strong confinement limit,* Nature Photonics, Vol. 1, pp. 57 - 60.

Bayat, K. & Safavi-Naeini, S. & Chaudhuri, S.K. (2007). *Polarization and thickness dependent guiding in the photonic crystal slab waveguide,* ,Optics Express, Vol. 15, Issue 13, pp. 8391-8400.

Bayat, K. & Safavi-Naeini, S. & Chaudhuri, S.K. (2009). *Ultra-compact photonic crystal based polarization rotator* ,Optics Express, Vol. 17, Issue 9, pp. 7145-7158.

Bayat, K. & Safavi-Naeini, S. & Chaudhuri, S.K. & Barough, M.F. (2009). *Design and simulation of photonic crystal based polarization converter* ,J. Lightwave Technol., Vol. 27, Issue 23, pp. 5483-5491.

Bayat, K. & Rafi, G.Z. & Shaker, G.S.A. & Ranjkesh, N. & Chaudhuri, S.K. & Safavi-Naeini, S. (2010). *Photonic-crsytal based polarization converter for terahertz integrated circuit*, Microwave Theory and Tech., IEEE Trans., Vol. 58, Issue 7, pp. 1976-1984.

Bayat, K. & Safavi-Naeini, S. & Chaudhuri, S.K. (2007). *Polarization and thickness dependent guiding in the photonic crystal slab waveguide,* ,Optics Express, Vol. 15, Issue 13, pp. 8391-8400.

Chan, P.S. & Tsang, H.K. & Shu, C. (2003). *Mode conversion and birefringence adjustment by focused-ion-beam etching for slanted rib waveguide walls,* Opt. Lett., Vol. 28, No. 21, pp. 2109-2111.

Deng, H. (2005). *Design and characterization of silicon-on-insulator passive polarization converter with finite-element analysis,* Ph.D Thesis, University of Waterloo.

El-Refaei, H & Yevick, D. (2003) *An optimized InGaAsP/InP polarization converter employing asymmetric rib waveguides*, J. Lightwave Tech., Vol. 21, No. 6, pp. 1544-1548.

Genereux, F. & Leonard, S.W. & Van Driel, H.M. (2001) *Large birefringence in two-dimensional photonic crystals,* Phys. Rev. B., Vol. 63, pp. 161101.

Heidrich, H. & Albrecht, P. & Hamacherm, M. & Nolting, H.P. & Schroeter, H. & Weinert, C.M. (1992) *Passive mode converter with a periodically tilted InP/GaInAsP rib waveguide,* IEEE Photon. Tech. Lett., Vol. 4, No. 1, pp. 34-36.

Huang, J.Z. & Scarmozzino, R. & Nagy, G. & Steel, M.J. & Osgood, R.M. (2000) *Realization of a compact and single-mode optical passive polarization conveter,* IEEE Photon. Tech. Lett., Vol. 12, No. 3, pp. 317-319.

Huang, W. & Mao, Z.M. (1992) *Polarization rotation in periodic loaded rib waveguides,* IEEE J. Lightwave Tech., Vol. 10, pp. 1825-1831.

Haung, W.P. & Chu, S.T. & Chaudhuri, S.K. (1992) *Scalar coupled-mode theory with vector correction,* IEEE J. Quantum Electron, Vol. 28, pp. 184-193.

Lui, W.W. & Magari, K. & Yoshimoto, N. & Oku, S. & Hirono, T. & Yokoyama, K. & Huang W.P. (1997) *Modeling and design of bending waveguide based semiconductor polarization rotators,* IEEE Photon Tech. Lett., Vol. 9, No. 10, pp. 1379-1381.

Lui, W.W. & Xu, C.L. & Hirono, T. & Yokoyama, K & Huang, W.P. (1998) *Full-vectorial wave propagation in semiconductor optical bending waveguides and equivalent straight waveguides,* IEEE J. Lightwave Tech., Vol. 16, No. 5, pp. 910-914.

Lui, W.W. & Hirono, T. & Yokomaya, K. & Huang, W.P. (1998) *Polarization rotator in semiconductor bending waveguides: A coupled-mode theory formulation,* J. Lightwave Tech., Vol. 16, No. 5, pp. 929-936.

Johnson, S.G. & Fan, S. & Villeneuve, P.R. & Joannopoulos, J.D. (1999) *Guided modes in photonic crystal slabs,* Phys. Rev. B, Vol. 60, No. 8, pp.5751-5758.

Mertens, K & Scholl, B. & Schmitt, H.J. (1998) *Strong polarization conversion in periodically loaded strip waveguide,* IEEE Photon. Tech. Lett., Vol. 10, pp. 1133-1135.

Mrozowski, M. (1997) *Guided electromagnetic waves: properties and analysis,* England: Research Studies Press Ltd./ John Wiley & Sons Inc.

Obayya, S.S.A & Rahman, B.M.A & El-Mikati, H.A. (2000) *Vector beam propagation analysis of polarization conversion in periodically loaded waveguides,* IEEE Photon. Tech. Lett., Vol. 12, pp. 1346-1348.

Rahman, B.M.A & Obayya, S.S.A. & Somasiri, N. & Rajarajan, M. & Grattan, K.T.V. & El-Mikathi, H.A. (2001) *Design and characterization of compact single-section passive polarization rotator,* J. Lightwave Tech., Vol. 19, No. 4, pp. 512-519.

Shani, Y. & Alferness, R. & Koch, T. & Koren, U. & Oron, M. & Miller, B. I. & Young, M.G. (1991) *Polarization rotation in asymmetric periodic loaded rib waveguides,* Appl. Phys. Lett., Vol. 59, pp. 1278-1280.

Snyder, A.W. & Love, J.D. (1983), *Optical Waveguide Theory*, London :Chapman & Hall.

Tzolov, V.P. & Fontaine, M. (1996) *A passive polarization converter free of longitudinally-periodic structures,* Optics Communications, Vol. 27, pp. 7-13.

Van Dam, C. & Spickman, L.H. & Van Ham, F.P.G.M. & Groen, F.H. & Van Der Tol, J.J.G.M. & Moerman, I. & Pascher, W.W. & Hamacher, M. & Heidrich, H. & Weinert, C.M. & Smit, M.K. (1996) *Novel compact polarization converters based on ultra short bend,* IEEE Photon. Tech., Vol. 8, No. 10, pp. 1346-1348.

Wang, Z. & Dai, D. (2008) *Ultrasmall Si-nanowire-based polarization rotator,* J. Opt. Soc. Am. B, Vol. 25, No. 5, pp. 747-753.

Watts, M.R. & Haus, H.A. (2005) *Integrated mode-evolution-based polarization rotators,* Opt. Lett., Vol. 30, Issue 2, pp. 138-140.

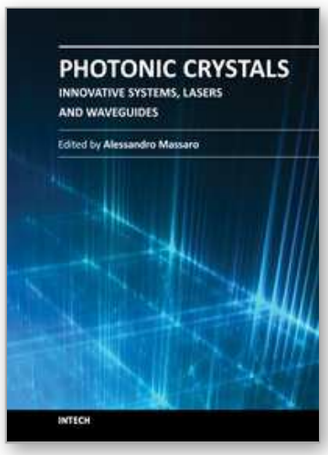


**Photonic Crystals - Innovative Systems, Lasers and Waveguides**

Edited by Dr. Alessandro Massaro

ISBN 978-953-51-0416-2
Hard cover, 348 pages
**Publisher** InTech
**Published online** 30, March, 2012
**Published in print edition** March, 2012

The second volume of the book concerns the characterization approach of photonic crystals, photonic crystal lasers, photonic crystal waveguides and plasmonics including the introduction of innovative systems and materials. Photonic crystal materials promises to enable all-optical computer circuits and could also be used to make ultra low-power light sources. Researchers have studied lasers from microscopic cavities in photonic crystals that act as reflectors to intensify the collisions between photons and atoms that lead to lazing, but these lasers have been optically-pumped, meaning they are driven by other lasers. Moreover, the physical principles behind the phenomenon of slow light in photonic crystal waveguides, as well as their practical limitations, are discussed. This includes the nature of slow light propagation, its bandwidth limitation, coupling of modes and particular kind terminating photonic crystals with metal surfaces allowing to propagate in surface plasmon-polariton waves. The goal of the second volume is to provide an overview about the listed issues.

**How to reference**

In order to correctly reference this scholarly work, feel free to copy and paste the following:

Bayat and Baroughi (2012). Photonic Crystal for Polarization Rotation, Photonic Crystals - Innovative Systems, Lasers and Waveguides, Dr. Alessandro Massaro (Ed.), ISBN: 978-953-51-0416-2, InTech, Available from: http://www.intechopen.com/books/photonic-crystals-innovative-systems-lasers-and-waveguides/polarization-behavior-of-photonic-crystal-slabs

INTECH
open science | open minds

**InTech Europe**
University Campus STeP Ri
Slavka Krautzeka 83/A
51000 Rijeka, Croatia
Phone: +385 (51) 770 447
Fax: +385 (51) 686 166
www.intechopen.com

**InTech China**
Unit 405, Office Block, Hotel Equatorial Shanghai
No.65, Yan An Road (West), Shanghai, 200040, China
中国上海市延安西路65号上海国际贵都大饭店办公楼405单元
Phone: +86-21-62489820
Fax: +86-21-62489821

IntechOpen